

Ellipticity of dark matter halos with galaxy-galaxy weak lensing

Rachel Mandelbaum^{1*}, Christopher M. Hirata¹, Tamara Broderick¹,
 Uroš Seljak^{1,2}, and Jonathan Brinkmann³

¹*Department of Physics, Jadwin Hall, Princeton University, Princeton NJ 08544, USA*

²*International Centre for Theoretical Physics, Strada Costiera 11, 34014 Trieste, Italy*

³*Apache Point Observatory, 2001 Apache Point Road, Sunspot NM 88349, USA*

2 October 2018

ABSTRACT

We present the results of attempts to detect the ellipticity of dark matter halos using galaxy-galaxy weak lensing with SDSS data. We use 2020 256 galaxies brighter than $r = 19$ with photometric redshifts (divided into colour and luminosity subsamples) as lenses and 31 697 869 source galaxies. We search for and identify several signal contaminants, which if not removed lead to a spurious detection. These include systematic shear that leads to a slight spurious alignment of lens and source ellipticities, intrinsic alignments (due to contamination of the source sample by physically-associated lens source pairs), and anisotropic magnification bias. We develop methods that allow us to remove these contaminants to the signal. We split the analysis into blue (spiral) and red (elliptical) galaxies. Assuming Gaussian errors as in previous work and a power-law profile, we find $f_h = e_h/e_g = 0.1 \pm 0.06$ for red galaxies and -0.8 ± 0.4 for blue galaxies using transverse separations of 20–300 h^{-1} kpc, averaged over luminosity. Inclusion of the more realistic non-Gaussian error distributions and of the NFW density profile (which predicts much smaller ellipticity of the shear for scales above the scale radius) yields 0.60 ± 0.38 for ellipticals and $-1.4^{+1.7}_{-2.0}$ for spirals. While there is no concrete detection of alignment in either case, there is a suggestion in the data of a positive alignment in the brightest lens sample of ellipticals. Our results appear to be mildly inconsistent with a previously reported detection by Hoekstra et al. (2004), but more data and further tests are needed to clarify whether the discrepancy is real or a consequence of differences in the lens galaxy samples used and analysis methods.

Key words: galaxies: haloes – gravitational lensing.

1 INTRODUCTION

Dark matter halo ellipticity, a robust prediction of Λ CDM according to N-body and hydrodynamic simulations, can in principle be detected using galaxy-galaxy weak lensing. In this paper, we attempt to detect the projected ellipticities of the dark matter halos of lens galaxies using data from the Sloan Digital Sky Survey (SDSS). Besides implications of such a detection for CDM and theories of hierarchical structure, a positive detection of halo ellipticity may also be used to constrain Modified Newtonian Dynamics, or MOND (Milgrom 1983; Sanders 1986; Sanders & McGaugh 2002), an alternative theory of gravity that describes rotation curves well without dark matter, but predicts an isotropic lensing signal around isolated galaxies at scales on

which there is no baryonic matter (though a combination of MOND and dark matter cannot be ruled out by this test).

Galaxy-galaxy weak lensing is a useful tool for studying the structure of dark matter halos on large scales. Because it is sensitive to all matter in the lenses, not just baryons, the signal (averaged over many lens and source galaxies) can be detected well beyond the extent of the light profiles, without the need for physically associated tracers such as satellite galaxies. At present, galaxy-galaxy weak lensing has been well-detected in several surveys (Brainerd et al. 1996; Hudson et al. 1998; Fischer et al. 2000; Smith et al. 2001; McKay et al. 2001; Guzik & Seljak 2002; Hoekstra et al. 2003; Sheldon et al. 2004; Hoekstra et al. 2004; Seljak et al. 2005a), with increasing statistical precision and gradually improving control of systematics (Mandelbaum et al. 2005a), and therefore may also be useful as a tool to study dark matter halo ellipticity.

* Electronic address: rmandelb@princeton.edu

Ellipticity of dark matter halo profiles has been predicted in CDM N-body simulations (e.g., Dubinski & Carlberg 1991), and observed with non-lensing methods on scales < 20 kpc (for a review, see Sackett 1999). Simulations typically predict triaxial halos with $b/a > 0.7$ and $c/a \sim 0.5$, where b/a is the ratio of intermediate to long axis, and c/a is the ratio of short to long axis. The resulting mean projected ellipticity is then 0.3. It should be noted, however, that simulations that include baryons show reduced halo ellipticity in the inner regions, with $\Delta(c/a)$ and $\Delta(b/a) \sim 0.1\text{--}0.4$ (Kazantzidis et al. 2004); the effect of baryons decreases with radius. One measurement of halo ellipticity using galaxy-galaxy weak lensing has already been reported. Hoekstra et al. (2004) argued for a detection of ellipticity by measuring $f_h = e_h/e_g$, the ratio of the dark matter halo ellipticity to the ellipticity of the light profile in projection, and found $f_h = 0.77^{+0.18}_{-0.21}$, nominally ruling out an isotropic lensing signal at the 99.5 per cent confidence level.

A measurement of dark matter halo ellipticity naturally depends on alignment between the ellipticity of the light distribution and of the matter distribution. Navarro et al. (2004) find, using gasdynamical simulations, that for spiral galaxies on small scales (within the virial radius) the disk spin axis is aligned with the minor axis of the dark matter halo, so when viewing the disks in projection we should see positive f_h . On larger scales ($1\text{--}2 h^{-1}\text{Mpc}$), when considering the alignment of the ellipticity of the light of spiral galaxies relative to large-scale structure, the reverse appears to be true, so that f_h should be negative on those scales. In contrast, comparison of N-body simulations of satellite distributions with the observed satellite distribution around the Milky Way (Libeskind et al. 2005; Zentner et al. 2005) suggest that its disk spin axis is aligned with the halo major axis, thus predicting a negative f_h on all scales. In short, predictions for spiral galaxies are conflicting. For elliptical galaxies, the halo and light ellipticities are expected to be aligned within the virial radius in the simplest models, giving positive f_h .

There are, however, a number of difficulties inherent in these measurements. Some are theoretical; for example, if the dark matter and light ellipticities are not well aligned, then any tendency for halo ellipticity will be undetectable. Likewise, as will be shown in §2.3, for some reasonable halo profiles, the ellipticity of the weak lensing signal is much less than the ellipticity of the projected matter distribution, so the signature of halo ellipticity in weak lensing is quite small. However, several effects are under our control: the statistics (i.e., finding a large enough sample that halo ellipticity effects, will be statistically significant); and PSF-related systematics, which may contaminate the halo ellipticity measurement, can be studied and understood.

The SDSS provides an excellent dataset on which to carry out these measurements by the above criteria. With 3×10^5 nearby ($z < 0.25$) galaxies with spectroscopy that can serve as lenses, or eight times as many bright ($r < 19$) lenses if we do not require spectroscopy, and roughly 3×10^7 fainter galaxies to serve as sources, the SDSS should provide the statistical power to measure these effects. Also, as will be described in §3.3, we have the tools to isolate the effects of PSF systematics on the halo ellipticity measurement.

We begin by outlining the weak lensing formalism and

the models used for the ellipticities of the dark matter halo in §2. Next, in §3, we describe the data used for these measurements and systematic effects that may bias the measurements. §4 outlines the method of analysis that we use to relate results from the data to our models in §2. Results are presented in §5, and the implications and suggestions for future work are in §6.

Here we note the cosmological model and units adopted for this work. Pair separations are measured in transverse comoving $h^{-1}\text{kpc}$ using the angular diameter distance (in a flat ΛCDM cosmology with $\Omega_m = 0.3$, $\Omega_\Lambda = 0.7$) at the lens redshift. In the units used, our results are independent of H_0 .

2 THEORY

2.1 Galaxy-galaxy weak lensing formalism

In this paper, we use the notation and approach to the lensing signal computation from Mandelbaum et al. (2005a), hereinafter M05. In this section we briefly mention the main points of the analysis.

Galaxy-galaxy weak gravitational lensing is sensitive to the differential surface density $\Delta\Sigma(r) = \bar{\Sigma}(< r) - \Sigma(r)$ (for an axisymmetric halo) averaged over many lenses. This surface density can be related to a product of a tangential shear term and a redshift-dependent term, $\Delta\Sigma = \gamma_t \Sigma_c$, where the critical surface density is defined in comoving coordinates via

$$\Sigma_c = \frac{c^2}{4\pi G} \frac{D_s}{D_{ls} D_l (1 + z_l)^2} \quad (1)$$

where D is the angular diameter distance, and l and s refer to the lens and source, respectively.

The tangential shear is computed by finding the average value of tangential ellipticity, but the two are related by a factor of 2 according to our definitions; furthermore, we must divide by a shear responsivity factor. We write

$$\Delta\Sigma = \frac{\sum_i w_i (e_t \Sigma_c)_i}{2\mathcal{R} \sum_i w_i} \quad (2)$$

where the summation is over lens-source pairs, \mathcal{R} is the shear responsivity which describes the effects of a shear on the tangential ellipticities (Bernstein & Jarvis 2002), and the weights are defined by

$$w_i = \frac{\Sigma_{c,i}^{-2}}{\sigma_{e_t,i}^2 + \sigma_{SN}^2}, \quad (3)$$

where the weighting is by inverse measurement noise plus shape noise. Since typical rms ellipticities are of order 0.36 and typical shears are of order 10^{-3} , we must average over millions of lens-source pairs to get reasonable signal to noise. The shear responsivity and weighting scheme are discussed in more detail in M05. Once these sums have been accumulated, we must subtract off the signal measured around random points, and boost by the number of pairs relative to the number around random points to account for dilution of the signal by physically-associated pairs.

2.2 Our Model

Here we describe the model used in this paper for halo ellipticity. This formalism was developed by Natarajan & Refregier (2000) and applied to the elliptical isothermal sphere density profile.

We attempt to determine a parameter f which is related to the ellipticity of $\Delta\Sigma$, the differential dark matter surface density of galaxies. We model $\Delta\Sigma$ as having an isotropic component $\Delta\Sigma_{iso}$ and some azimuthal variation as follows:

$$\Delta\Sigma_{model}(r) = \Delta\Sigma_{iso}(r) [1 + 2f e_g \cos(2\Delta\theta)] \quad (4)$$

where e_g is the observed ellipticity of the light distribution of the lens and $\Delta\theta$ is the angle from the lens major axis. We can determine $\Delta\Sigma_{iso}$ and f by minimizing

$$\chi^2 = \frac{\sum_i w_i (\Delta\Sigma_{model} - \Delta\Sigma_i)^2}{\sum_i w_i} \quad (5)$$

where the summation is over lens-source pairs denoted by i with weights described in §2.1 and $\Delta\Sigma_i = e_{t,i} \Sigma_c$ for the pair i . By minimizing with respect to f and $\Delta\Sigma_{iso}$, we obtain the following joint solution for the two quantities¹:

$$\begin{aligned} \Delta\Sigma_{iso}(r) &= \frac{\sum_i w_i \Delta\Sigma_i}{\sum_i w_i} \quad (6) \\ f \Delta\Sigma_{iso}(r) &= \frac{\sum_i w_i \Delta\Sigma_i e_{g,i} \cos(2\Delta\theta_i)}{2 \sum_i w_i e_{g,i}^2 \cos^2(2\Delta\theta_i)} \end{aligned}$$

The solution for $\Delta\Sigma_{iso}(r)$ is thus as expected, the usual averaging of tangential ellipticity over all pairs, and the calculation of $f \Delta\Sigma_{iso}(r)$ is a summation weighted by $e_g \cos(2\Delta\theta)$, which will pick out any tendency for $\Delta\Sigma$ to be larger (smaller) along the major axis of the projected light distribution, yielding a positive (negative) value for $f \Delta\Sigma_{iso}(r)$. This procedure can be used even if f is not a constant with radius, allowing us to measure $f(r) \Delta\Sigma_{iso}(r)$.

We also will find it necessary to calculate $\Delta\Sigma_{45}$, the signal with source ellipticities rotated by $\pi/4$. While this quantity must average out to zero by symmetry when averaged over $\Delta\theta$, we will see in §2.3 that it can have a $\sin(2\Delta\theta)$ dependence. If we also rotate the lens ellipticities in the same direction as the source ellipticities, that $\sin(2\Delta\theta)$ dependence becomes a $\cos 2\Delta\theta$ dependence as for the tangential shear, i.e.

$$\Delta\Sigma_{45,model}(r) = \Delta\Sigma_{iso}(r) [2f_{45} e_g \cos(2(\Delta\theta + \pi/4))] \quad (7)$$

so we can write

$$f_{45} \Delta\Sigma_{iso}(r) = \frac{\sum_i w_i \Delta\Sigma_{i,45} e_{g,i} \cos[2(\Delta\theta_i + \pi/4)]}{2 \sum_i w_i e_{g,i}^2 \cos^2[2(\Delta\theta_i + \pi/4)]}. \quad (8)$$

Once these sums have been calculated, the usual prescription must be followed as already described: divide by $2\mathcal{R}$, subtract off the random catalog signal from $\Delta\Sigma_{iso}$, and multiply by the boost factor $B(r)$, the ratio of lens-source pairs using real lenses to the number using random points as lenses, which goes to one in the limit of no physically associated sources included in the sample, and is larger than

¹ This results in minimization if $\sum_i w_i e_{g,i} \cos(2\Delta\theta_i)$ is negligibly small, as would be expected if the sources are isotropically distributed relative to the lens major axis. The validity of this approximation is extensively discussed in §3.3.2.

that at small transverse separations. Multiplying by this factor corrects the signal for dilution due to these non-lensed galaxies included in the source sample.

There are a number of difficulties to consider when attempting to detect dark matter halo ellipticity that complicate this simple model we have presented here, in particular difficulties in getting adequate signal to noise, the question of whether the light and mass ellipticities are actually aligned, choosing radial ranges to best carry out this measurement, and systematics that obscure the measurement. All of these issues will be addressed in the sections that follow.

2.3 Connection to theory and other work

In order to facilitate a comparison of our results with theory and with observational results from Hoekstra et al. (2004), we must relate the quantities we measure to theoretical predictions for various halo density profiles.

We consider several different types of profiles. The simplest is the general power-law profile, for which we derive analytic expressions for f correct to first order in the ellipticity. More realistic profiles, particularly the Truncated Isothermal Sphere (TIS) and the Navarro-Frenk-White (NFW) profile, are also considered, with numerical results given. In all cases, we introduce ellipticity by replacing r in the isotropic form for $\kappa(r)$ with an elliptical coordinate to compute (analytically or numerically) the potential and, ultimately, the shears $\gamma_t(r)$ and $\gamma_{45}(r)$. We find that the degree to which the ellipticity of κ is expressed as ellipticity of $\Delta\Sigma$ depends on the shape of the profile.

For a dark matter halo with power-law space density profile $\rho(r) \propto r^{-(1+\alpha)}$ and ellipticity independent of radius e_h , oriented with major axis along $\theta = 0$ and π for simplicity, we can write the surface density as

$$\kappa(r, \theta) = A \left[r \left(1 - \frac{e_h}{2} \cos(2\theta) \right) \right]^{-\alpha} \quad (9)$$

$$\cong A r^{-\alpha} \left[1 + \frac{e_h \alpha}{2} \cos(2\theta) \right]. \quad (10)$$

This definition ensures that for major axis a and minor axis b , the relationship $e_h = (a^2 - b^2)/(a^2 + b^2)$ holds. The next order term, proportional to $\cos^2(2\theta)$, has a coefficient that is smaller than that of the $\cos(2\theta)$ term by a factor of $e_h(1 + \alpha)/4$, which for typical values $\alpha \sim 1$ and $e_h \sim 0.3$ is roughly 0.15. Consequently we will ignore all terms of order higher than $\cos 2\theta$ for the remainder of this calculation.

For an axisymmetric (around the line of sight) matter distribution, we could simply obtain $\Delta\Sigma$ by finding the average value of κ within radius r and using $\Delta\Sigma = \Sigma_c [\bar{\kappa}(<r) - \kappa(r)]$. However, for non-axisymmetric halos, we must do the full calculation, first determining the lensing potential corresponding to the surface density via

$$\kappa = \frac{1}{2} \nabla^2 \Phi = \frac{1}{2} \left[r^{-1} \frac{\partial}{\partial r} \left(r \frac{\partial \Phi}{\partial r} \right) + r^{-2} \frac{\partial^2 \Phi}{\partial \theta^2} \right]. \quad (11)$$

With an ansatz of $\Phi = \sum_m \Phi_0(m) r^{-\beta(m)} \cos(m\theta)$, our first order approximation (Eq. 9) gives a potential of

$$\Phi(r, \theta) = \frac{2A}{(\alpha - 2)^2} r^{2-\alpha} \left[1 + \frac{B(\alpha - 2)^2}{\alpha(\alpha - 4)} \cos(2\theta) \right] \quad (12)$$

where $B = e_h \alpha / 2$. Since this expression diverges for $\alpha = 2$

($\rho \propto r^{-3}$), it cannot be used to derive expressions for the shear and f for NFW profiles well beyond the scale radius.

We can then use the potential to determine γ_t and γ_{45} via

$$\gamma_t(r, \theta) = \frac{1}{2} \left(-\frac{\partial^2 \Phi}{\partial r^2} + r^{-1} \frac{\partial \Phi}{\partial r} + r^{-2} \frac{d^2 \Phi}{d\theta^2} \right) = \kappa - \frac{d^2 \Phi}{dr^2} \quad (13)$$

$$\gamma_{45}(r, \theta) = -r^{-1} \frac{\partial^2 \Phi}{\partial \theta \partial r} + r^{-2} \frac{\partial \Phi}{\partial \theta}$$

For a general power-law potential, we therefore find

$$\gamma_t = \frac{\alpha}{2 - \alpha} Ar^{-\alpha} \left[1 + \frac{(\alpha - 2)(\alpha^2 - 2\alpha + 4)B}{\alpha^2(\alpha - 4)} \cos(2\theta) \right] \quad (14)$$

$$\gamma_{45} = \frac{\alpha}{2 - \alpha} Ar^{-\alpha} \left[\frac{4(2 - \alpha)(1 - \alpha)B}{\alpha^2(\alpha - 4)} \right] \sin(2\theta)$$

We can then make the identification $\Delta\Sigma_{iso}(r) = \Sigma_c \alpha Ar^{-\alpha} / (2 - \alpha)$ to relate back to our model in Eq. 4.

In the special case of an elliptical SIS ($\alpha = 1$), we have $d^2\Phi/dr^2 = 0$, $\gamma_t = \kappa$, and therefore

$$\gamma_t = Ar^{-1} \left[1 + \frac{e_h}{2} \cos(2\theta) \right] \quad (15)$$

$$\gamma_{45} = 0$$

Comparison against our model in Eq. 4 shows that our $f = e_h/4e_g$, so that for $e_h = e_g$ ($f_h = 1$) we expect $f = 0.25$. Dividing the measured f by the predicted SIS value $f/f_h = 0.25$ then allows us to compute the measured f_h from our f value assuming the SIS density profile.

More generally, for a power-law non-SIS model, we find

$$f = \frac{f_h}{4} \left[\frac{(\alpha - 2)(\alpha^2 - 2\alpha + 4)}{\alpha(\alpha - 4)} \right] \quad (16)$$

so for $\alpha = 0.8-0.9$ (a typical value in the actual data at small transverse separations) $f \sim 0.33f_h$.

We are also interested in computing f_{45} for these profiles. By comparison with previous equations, we find

$$f_{45} = f_h \left[\frac{(2 - \alpha)(1 - \alpha)}{\alpha(\alpha - 4)} \right] = \frac{4(\alpha - 1)}{\alpha^2 - 2\alpha + 4} f \quad (17)$$

Consequently the expected signal with lenses and sources rotated by $\pi/4$ can be predicted relative to the unrotated signal, and the comparison of the two is an important consistency check. For $\alpha \sim 0.8-0.9$ as is found in the data, $f_{45}/f \sim -0.26$ to -0.13 , i.e. the rotated signal is smaller than the unrotated one and with opposite sign. As will be described in §3.3, to eliminate contributions from systematics to $f\Delta\Sigma$, we actually will measure $f - f_{45}$, which for the general power-law profile is

$$f - f_{45} = \frac{(\alpha - 2)(\alpha - 4)}{\alpha^2 - 2\alpha + 4} f = \frac{f_h}{4} \left[\frac{(\alpha - 2)^2}{\alpha} \right] \quad (18)$$

We also consider non-power law density profiles. The first such profile that we will consider is the TIS (Brainerd et al. 1996), which takes the form

$$\rho(r) \propto \frac{1}{r^2(r_s^2 + r^2)} \quad (19)$$

(note that what we call r_s here is often called s ; we use r_s for simplicity of notation since it also appears in the NFW

profile). This profile yields $\kappa \propto r^{-1}$ for $r \ll r_s$ and $\propto r^{-3}$ for $r \gg r_s$. While analytic expressions can be derived for the shear in the spherical case, numerical integration must be used when r is replaced by an elliptical coordinate. Fortunately, κ and γ can be computed for this model using GRAVLENS² (Keeton 2001) via subtraction of the shear from an elliptical $\kappa \propto (r^2 + s^2)^{-1/2}$ model from a $\kappa \propto r^{-1}$ model (due to linearity of the shear), with r being replaced by an elliptical coordinate. We can use the predictions for those quantities to compute $f - f_{45}$ by finding, for a profile with ellipticity e ,

$$\begin{aligned} \Delta(r) &\equiv \gamma_t(r, \theta = 0) - \gamma_t(r, \theta = \pi/2) \\ \Delta_{45}(r) &\equiv \gamma_{45}(r, \theta = \pi/4) - \gamma_{45}(r, \theta = 3\pi/4) \\ T(r) &\equiv \gamma_t(r, \theta = 0) + \gamma_t(r, \theta = \pi/2) \\ f(r) &= \frac{\Delta(r)}{2eT(r)} \\ f_{45}(r) &= \frac{\Delta_{45}(r)}{2eT(r)} \end{aligned} \quad (20)$$

The plot in Fig. 1 shows the results for f , f_{45} , and $f - f_{45}$ as a function of r/r_s for the TIS over a wide range of scales. (This plot was computed using $e = 0.02$, for which the variation of the shear with azimuthal angle is dominated by the first-order $\cos(2\theta)$ term; at more realistic values like $e = 0.3$, higher order terms may contribute as much as 18 per cent of the value of this first order term. However, as will be shown, since our results include statistical uncertainty larger than this value, we will henceforth neglect higher order terms.) Notice that f for the TIS is a declining function of transverse separation, and for the smallest scales shown on the plot approaches the SIS prediction $f/f_h = 0.25$. Because f_{45} is so large, $f - f_{45}$ is quite close to zero for $r \sim 0.6r_s$ to the largest scales shown on the plot, $r \sim 3r_s$.

We also consider the NFW profile (Navarro et al. 1996), which takes the form

$$\rho = \frac{\rho_s}{(r/r_s)(1 + r/r_s)^2}, \quad (21)$$

where $r_s = r_v/c$ (concentration parameter). While the shear for the spherical NFW model can be computed analytically (Wright & Brainerd 2000), the additional complication of ellipticity necessitates the use of numerical integration to get the shear. So, we again use γ from GRAVLENS to compute f and f_{45} . A plot of $f(r)$ for this model is shown in Fig. 2. As shown, the NFW model gives decreasing $f(r)$ as for the TIS model. While at $r = r_s$, the NFW model gives $f/f_h \sim 0.3$ (slightly larger than the SIS) and $f_{45} \ll f$, f decreases at larger radii and f_{45} increases so that $f - f_{45}$ is quite small for r larger than about $2r_s$.

For the sake of clarity, Table 1 summarizes the definitions of all ellipticity-related parameters used in this paper.

3 DATA

The data used for this paper come from the Sloan Digital Sky Survey, or SDSS (York et al. 2000), an ongoing survey

² The latest version may be found via the link at <http://cfa-www.harvard.edu/castles/>.

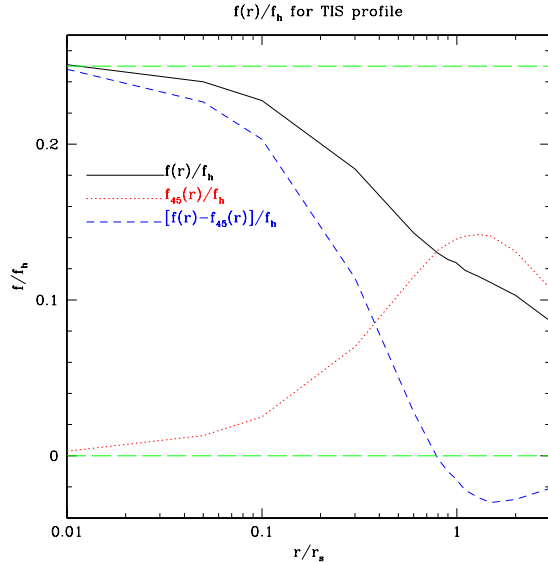


Figure 1. Plot of predicted $f(r)/f_h$ and $f_{45}(r)/f_h$ for an elliptical TIS density profile dark matter halo; the maximum radius shown, $3r_s$, is larger than the scales used in this paper. Horizontal lines indicate the SIS predictions $f/f_h = 0.25$ and $f_{45}/f_h = 0$.

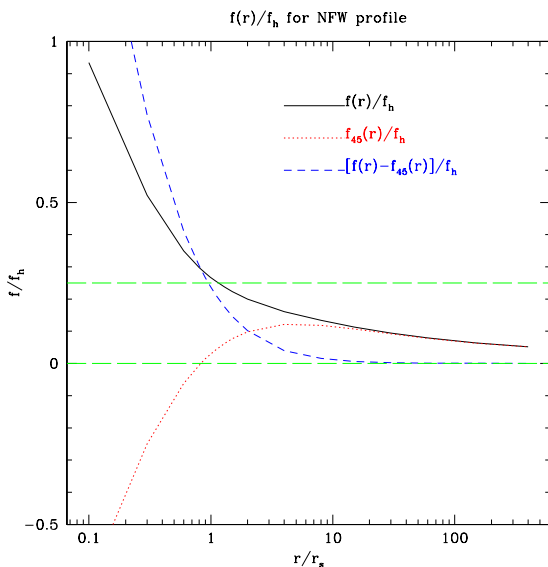


Figure 2. Plot of predicted $f(r)/f_h$ and $f_{45}(r)/f_h$ for an elliptical NFW density profile dark matter halo. Horizontal lines indicate the SIS predictions $f/f_h = 0.25$ and $f_{45}/f_h = 0$.

that will eventually image approximately one quarter of the sky (10,000 square degrees). Imaging data is taken in drift-scan mode in 5 filters, *ugriz*, centred at 355, 469, 617, 748, and 893 nm respectively (Fukugita et al. 1996, Smith et al. 2002) using a wide-field CCD (Gunn et al. 1998) with photometric monitor (Hogg et al. 2001). After the computation of an astrometric solution (Pier et al. 2003), the imaging data are processed by a sequence of pipelines, collectively called PHOTO, that estimate the PSF and sky brightness, identify objects, and measure their properties. The software pipeline and photometric quality assessment is de-

Table 1. Definitions of all measures of projected ellipticities (of dark matter halo and source distributions) used in this paper.

f	Ellipticity of $\Delta\Sigma = \Delta\Sigma_{iso}[1 + 2fe_g \cos(2\Delta\theta)]$
f_h	Ellipticity of halo relative to light distribution, e_h/e_g
f_{45}	Ellipticity of $\Delta\Sigma_{45} = 2f_{45}\Delta\Sigma_{iso}e_g \sin(2\Delta\theta)$
f_γ	Ellipticity of shear before boosting; $\neq f$ if boost has azimuthal dependence
f_{int}	Ellipticity of distribution of physically-associated ‘‘sources’’
f_{mag}	Ellipticity of magnification bias $\delta N/N \propto \kappa \propto (1 + 2f_{mag}e_g \cos(2\Delta\theta))$
f_{eff}	Effective ellipticity of f_{int} , f_{mag} taking into account dilution by isotropic source distribution

scribed in Ivezić et al. (2004). Bright galaxies and other interesting objects are selected for spectroscopy according to specific criteria (Eisenstein et al. 2001; Strauss et al. 2002; Richards et al. 2002). The SDSS has had four major data releases: the Early Data Release or EDR (Stoughton, et al. 2002), DR1 (Abazajian et al. 2003), DR2 (Abazajian et al. 2004), and DR3 (Abazajian et al. 2005).

The lens and source catalogs are very similar to those described in M05, except for the inclusion of the fainter lenses with photometric redshifts. Thus the description here will be brief, with the exception of the few differences from that work which will be described in more detail.

3.1 Lens sample

While M05 used only 3×10^5 spectroscopic galaxies ($r < 17.77$) as lenses, this work uses a larger sample of 2 million lenses as faint as $r = 19$ (model magnitude) with photometric redshifts from KPHOTOZ v3.2 (Blanton et al. 2003a) in the range $0.02 < z < 0.5$. There are several reasons for this change. First, in order to detect a possibly small azimuthal variation in the tangential ellipticity, we need a much larger sample of lenses. Because of the higher number density of lenses when we include these fainter lenses, and because of the larger photometric area coverage, the use of a fainter flux limit increases the size of our lens sample by a factor of roughly eight. Second, while a lensing analysis aimed at determining the signal amplitude suffers from significant calibration uncertainty when galaxies without spectroscopic redshifts are used as lenses (Kleinheinrich et al. 2005), this work is primarily concerned with the ratio of $f\Delta\Sigma$ to $\Delta\Sigma$, so errors in signal calibration are irrelevant.

There is one possible error in the detection of f that could be affected by the use of photometric redshifts. The photometric redshifts are used for each lens to determine $D_A(z)$ and consequently the transverse separation between lenses and sources. If f is a constant value independent of radius for the projected mass distribution, then errors in the computed transverse separation do not matter, since they will affect $\Delta\Sigma$ and $f\Delta\Sigma$ in the same way. However, if f decreases with radius, and errors in the photometric redshifts tend to go in one direction (nonzero average bias), then the measured f can be systematically affected. If the photometric redshifts tend to be biased high, then they will

Table 2. For each luminosity bin, the number of lens galaxies, $\langle z \rangle$, and $\sigma(z)$ (a characteristic width, though the distribution is not Gaussian), the mean weighted redshift z_{eff} , and the mean weighted luminosity L_{eff} relative to L_* . The mean weighted redshifts differ for the different source samples, and the results shown are the average of those values.

Sample, M_r range	N_{gal}	$\langle z \rangle$	$\sigma(z)$	z_{eff}	L_{eff}/L_*
Blue lenses					
L3, $[-20, -19]$	215 808	0.12	0.04	0.12	0.5
L4, $[-21, -20]$	310 161	0.19	0.05	0.17	1.1
L5, $[-22, -21]$	145 136	0.27	0.09	0.23	2.5
L6, $[-23, -22]$	38 683	0.37	0.11	0.27	6.3
Red lenses					
L3, $[-20, -19]$	232 446	0.13	0.04	0.12	0.5
L4, $[-21, -20]$	538 364	0.18	0.05	0.17	1.2
L5, $[-22, -21]$	431 775	0.25	0.08	0.23	2.6
L6, $[-23, -22]$	107 883	0.34	0.10	0.26	5.9

overestimate the value of r , and lead to an overestimate of f ; if they are biased low, they will underestimate the value of r and consequently of f . Were it not for this problem, we would make a larger lens sample by going to fainter magnitudes, but the bias and scatter in the photometric redshifts at fainter magnitudes makes this impractical. As shown in M05 using data from DEEP2, for $r < 19$, the photometric redshifts are not noticeably biased, and have scatter $\Delta z \sim 0.04$. Since $D_A(z)$ is not linear in redshift and f is not linear in r , in principle even with no bias and a scatter of $\Delta z \sim 0.04$, the errors in r may bias our results, since we use $r = \theta D_A(z)(1+z)$. However, calculations indicate that this potential bias is well below the statistical error.

The area covered by the full catalog is roughly 6200 square degrees. Shape measurements were obtained for roughly 96 per cent of lenses passing the magnitude cut in this region, where many of the failures were due to saturated centres or other problems for very bright galaxies.

The lenses were split into luminosity bins one model magnitude wide; the notation for the bins here is the same as in M05, but we only use the four brightest bins from that paper, for which the signal was detected with high signal-to-noise. The luminosities were computed using the photometric redshift to get the distance modulus, and k-corrections are from KCORRECT v1.11 (Blanton et al. 2003a). As in M05, a luminosity evolution correction consistent with Blanton et al. (2003b) was applied, shifting all r -band magnitudes by $+1.6(z - 0.1)$. Table 2 includes information about the luminosity bins, including the numbers of lenses and parameters of the redshift and magnitude distribution. The effective redshifts and luminosities are computed using the same weights as are used in the computation of the lensing signal. Information is shown for red and blue samples separately, where colour separation will be described shortly.

In addition to the real lens catalog, our analysis also requires catalogs of random lens positions. These were created by distributing the random lenses uniformly across the survey area, since the photometric survey at $r < 19$ is fairly uniform and the density of sources at bright magnitudes does not vary significantly with seeing (at fainter magnitudes, where star/galaxy separation is more difficult, the

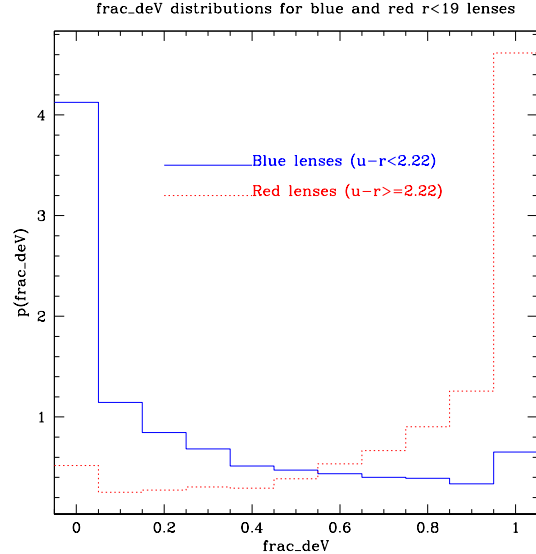


Figure 3. The distribution of `frac_deV` values for red and blue samples of galaxies, respectively

density of sources does not show the expected increase with magnitude, and shows significant variation with seeing).

It is also necessary to split the lens sample approximately into elliptical and spiral samples. For this purpose, we used the observed $u - r$ (model) colour, with a division at 2.22 as in Strateva et al. (2001). As a check of this colour separator, we used an independent method of classifying morphology, the `frac_deV` parameter output by PHOTO which, for each band, is determined by fitting the profile to `frac_deV` times the best-fit deVaucouleurs profile plus $1 - \text{frac_deV}$ times the best-fit exponential profile, and truncating the allowed range of values at 0 and 1. This procedure is done in each band; we use the r band result due to its high signal to noise. Thus, `frac_deV` is determined only via the profile shape in one band, not from the colour. Fig. 3 shows the distribution of `frac_deV` values for the red versus for the blue galaxies; as shown, the distribution for blue galaxies is strongly peaked at zero and for red galaxies at one, as would be expected if red colours and deVaucouleurs profiles are correlated, and if blue colours and exponential profiles are correlated. Hence we conclude that our “blue” and “red” samples include relatively pure samples (at the ~ 90 per cent level) of spiral and elliptical galaxies respectively.

3.2 Source sample

The source catalog is the same as in M05. In brief, shape measurements were performed on all SDSS imaging data collected through June 2004, using the re-Gaussianization technique described in Hirata & Seljak (2003), yielding roughly 3×10^7 source galaxies. Star-galaxy separation was achieved using PHOTO output OBJC_TYPE, and galaxies were required to meet the following criteria: no flags from PHOTO indicating problems with object measurement (e.g., a saturated centre) can be set, r band extinction less than 0.2, r band extinction-corrected model magnitude $r < 21.8$, resolution factor $R_2 > 1/3$ in both bands (r and i) used for the shape measurement to ensure high-quality shape mea-

measurements and to eliminate stars that were mis-classified by OBJC_TYPE as galaxies. For the purpose of the calculation of the shear signal, there are 3 disjoint sets of sources: “bright” ($r < 21$) sources, “faint” ($21 < r < 21.8$) sources, and high-redshift ($0.4 < z < 0.65$) Luminous Red Galaxies, or LRGs, which are explicitly excluded from the other two samples. The shear calibration was found in M05 to be accurate to within $[-7, +12]$ per cent (2σ level) for $r < 21$ sources, $[-10, +18]$ per cent for $r > 21$ sources, and $[-8, 19]$ per cent for high-redshift LRGs. Redshift distributions were determined for faint ($r > 21$) sources using DEEP2 spectroscopy (Davis et al. 2003, Madgwick et al. 2003, Davis et al. 2004, Coil et al. 2004), whereas redshift estimates for individual galaxies were obtained for the other two source samples. For the bright ($r < 21$) sources, photometric redshifts from KPHOTOZ v3.2 (Blanton et al. 2003a) with error distributions determined using DEEP2 spectroscopy in M05 were used; LRG photometric redshifts with error distributions from Padmanabhan et al. (2005) were used for the LRG sample.

3.3 Systematics

In M05, a large number of systematic errors in the weak lensing signal were analyzed to assess their significance in the SDSS data. For this work, many of the calibration uncertainties considered there (e.g., shear calibration bias, redshift distribution systematics, and stellar contamination) are irrelevant due to our interest in the ratio of $f\Delta\Sigma$ to $\Delta\Sigma$, both of which have the same calibration biases. However, there are other, more subtle systematics that are important here, that we describe in the subsections that follow.

3.3.1 Systematic shear

One possible contaminant of the f measurement is systematic shear. As discussed in M05, any average smearing of the images along the scan direction will cause a slight alignment of the lens and source ellipticities. This systematic thus raises (lowers) the shear signal on large scales by an additive factor if the PSF correction scheme over- (under-)estimates the correction to the shears due to this smearing. A constant systematic shear only changes $\Delta\Sigma$ on large scales, because for an isotropic distribution of sources around a lens, all contributions from the systematic shear to the tangential ellipticities cancel out; consequently, it is only important for lenses with an anisotropic distribution of sources. Fortunately, as described there, we can correct for the effects of systematic shear in the lensing signal using random lens catalogs to compute the signal due to systematic shear, so that we can subtract it off from the real signal.

Unfortunately, for the $f\Delta\Sigma$ measurement, this procedure is insufficient. The alignment of lens and source ellipticities due to systematic shear will lower $f\Delta\Sigma$ (since $\gamma_{t,sys} < 0$ where $\cos(2\Delta\theta) > 0$, and vice versa) thus lowering our estimate of f . This signal cannot be calculated analytically and removed without a very well-understood model for the size of the systematic shear and its variation on the sky (which we lack). However, there is one way to measure it: the systematic shear contributes equally to $f\Delta\Sigma$ and to $f_{45}\Delta\Sigma$ (since rotating the lens and source ellipticities by the same angle

does not change the fact that they are aligned). Since the spurious shear contributions to $f_{45}\Delta\Sigma$ and $f\Delta\Sigma$ are equal, we can subtract $f_{45}\Delta\Sigma$ from $f\Delta\Sigma$ to measure the uncontaminated value of $(f - f_{45})\Delta\Sigma_{iso}$, for which we presented model predictions in §2.3. As theoretical justification for the subtraction to eliminate systematics, we note that the shear correlation functions are related via

$$\xi_{++}(\theta) \pm \xi_{xx}(\theta) = \frac{1}{2\pi} \int \ell d\ell [P_E(\ell) \pm P_B(\ell)] \begin{cases} J_0(\ell\theta) \\ J_4(\ell\theta) \end{cases}. \quad (22)$$

Here, ξ_{++} and ξ_{xx} , the correlation functions of tangential and 45-degree rotated shear, are related via multiplicative factors to the measured $f\Delta\Sigma$ and $f_{45}\Delta\Sigma_{45}$ (respectively) resulting from systematic shear, P_E is the power spectrum of the E -mode contribution to systematic shear, and P_B is the power spectrum of the B -mode systematic shear. On small scales ($\ell\theta \ll 1$, so $J_0 \rightarrow 1$ and $J_4 \rightarrow 0$), $\xi_{++} = \xi_{xx}$, i.e. the contribution of a constant systematic shear to $f\Delta\Sigma$ and $f_{45}\Delta\Sigma$ is identical. As we will see, the signal from the systematic shear is indeed consistent with being associated with scales larger than those we use for the halo ellipticity measurement, justifying our scheme for eliminating this systematic.

3.3.2 Anisotropic source number density

In this paper, we are primarily concerned with transverse separations from $20 h^{-1}\text{kpc}$ (the minimum scale at which signal is measured) to several hundred $h^{-1}\text{kpc}$, around the virial radius. For our measurement, we use a boost factor $B(r)$ (to account for dilution of the signal due to inclusion of non-lensed galaxies in the source sample) that is azimuthally averaged, and therefore does not include variations of the observed galaxy number density with $\Delta\theta$. We consider here four effects that may cause azimuthal variation of the number density of galaxies around lenses, and their implications for our measurement of halo ellipticity using an azimuthally-averaged $B(r)$: anisotropic magnification bias, sky subtraction errors, density-shape intrinsic alignments, and the inclusion of foregrounds in the source sample.

The first such concern that can cause azimuthal variation of the source galaxy density is magnification bias, the effect of which is determined for each source sample as described in section 4.7.3 of M05. The magnification bias on average affects the amplitude of both $\Delta\Sigma$ and $f\Delta\Sigma$ by an overall factor (since we boost by $1 + \xi_{ts}$ determined using random catalogs, and therefore we are assuming that some of the real sources visible due solely to magnification bias are not lensed, so we overestimate the average signal). However, since magnification bias causes $\delta N/N \propto \kappa$, and κ varies azimuthally in our model, we must ask whether our use of azimuthally-averaged $B(r)$ biases the measurement of f_h . If the ellipticities of light and dark matter are aligned, then the magnification bias anisotropy will increase the source density along the lens major axis more than along the minor axis. This effect can be modeled as an isotropic background of sources that would be seen in the absence of lensing, plus an isotropic distribution of physically associated sources, which together give us a boost factor $B_{iso}(r)$. Magnification bias leads to some additional boost factor, $B_{mag}(r)[1 + 2f_{mag}e_g \cos(2\Delta\theta)]$. However, in reality these

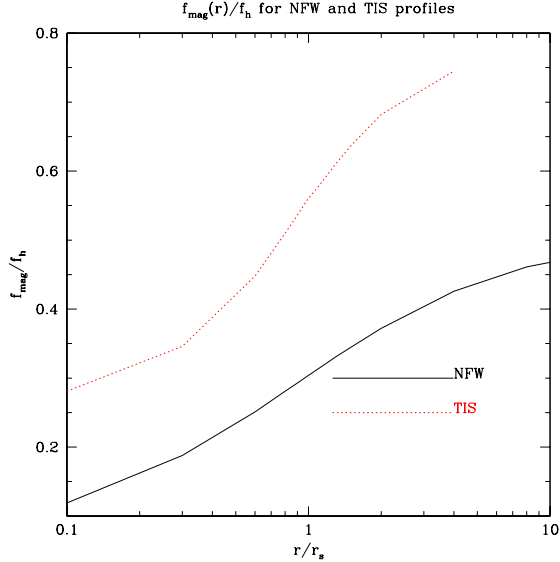


Figure 4. $f_{mag}(r)$ for the NFW and TIS models as a function of of transverse separation, in units of scale radii.

extra sources along the major axis are truly lensed, so there is no need for our boost factor to have azimuthal variation to account for the azimuthal variation in source number density. Therefore, in the presence of anisotropic magnification bias, our use of the angle-averaged $B(r) = B_{iso}(r) + B_{mag}(r)$ will overestimate the lensing signal, biasing both $\Delta\Sigma$ and $f\Delta\Sigma$, but not f_h .

While anisotropy of the source distribution around lenses due to magnification bias does not bias the measurement of f using an azimuthally-averaged boost factor, it does provide an interesting test of our results if we can detect it, because the values of f and f_{mag} are related to f_h in a consistent way by the halo density profile $\rho(r)$. As shown in Eq. 9, for a purely power-law profile, $f_{mag} = f_h\alpha/4$. Fig. 4 shows f_{mag} as a function of scale for NFW and TIS profiles. When studying our results in §5 we will return to the issue of detecting anisotropy of magnification bias.

The second effect we discuss that may cause number density anisotropy is small-scale errors due to PHOTO, the sky subtraction systematic described in section 6.3.7 of M05. In short, a problem with determination of the sky level near bright ($r < \sim 17.5$) lenses leads to variation of galaxy density within about $1'$ due to errors in the sky flux scattering galaxies into or out of our flux and apparent size cuts. Furthermore, model fits to determine fluxes and shapes are influenced in a difficult to quantify way. Consequently, we cannot assume an error in the amplitude of $\Delta\Sigma$ due to this effect that would cancel out of the ratio $(f\Delta\Sigma)/\Delta\Sigma$, we must ask whether it will induce alignments of densities on small scales that would change $f\Delta\Sigma$ but not $\Delta\Sigma$. Furthermore, we must consider that this effect depends on the angle from the lens major axis, since at fixed transverse separations, the light on the major axis is brighter than on the minor axis. Fortunately, the analysis is simplified by the fact that in our $r < 19$ lens sample used for this work, only about 17 per cent are at $r < 17.5$ where this effect is a problem.

We may naively expect that if the sky systematic acts only affects number counts in our catalog, then they will be

changed more on the major axis than on the minor axis. However, this systematic affects both lensed and physically-associated galaxies in the source sample, so dilution due to physically-associated sources should not have azimuthal dependence. Consequently, our use of azimuthally-averaged $B(r)$ is indeed appropriate.

The third effect we consider is the effect of intrinsic alignments. There are two intrinsic alignment effects that must be taken into account; the first is a correlation between the shapes of physically-associated galaxies, or the “shape-shape” correlation; the second effect is a correlation between the shapes of galaxies with the local density field, or the “density-shape” correlation. In this section we focus on the “density-shape” correlation, since it modulates the observed galaxy density around the lenses, and defer discussion of the “shape-shape” correlation for the next section.

While we attempt to eliminate physically-associated sources from our calculation using photometric redshifts for the $r < 21$ sample, the fact that our boost factors are greater than one indicates that we are not fully successful. If the distribution of physically-associated sources around lenses is not isotropic, but is instead aligned with the lens major axis, then the number density of “sources” on the sky may also appear to have such an alignment due to contamination. Such an effect is caused by an alignment between the lens galaxy shape and the local density field. This anisotropy of the satellite distribution has actually been detected before, albeit with conflicting amplitude and sign. The initial detection by Holmberg (1969), which gave rise to the name “the Holmberg effect,” was of an alignment of satellite galaxies along the minor axis of disk galaxies to transverse separations of 50 kpc. Since then, several studies have shown a similar effect: Zaritsky et al. (1997) found alignment of satellites along the minor axis of spiral galaxies for separations of 300-500 kpc, and Sales & Lambas (2004) found the same using a mixed sample of satellites in the 2-degree Field survey (2dF) out to 500 kpc. Other studies have shown the opposite; for example, Brainerd (2005), using a sample of satellites in the SDSS to projected separations of $400 h^{-1}$ kpc, found an alignment along the major axis; Mandelbaum et al. (2006) found a larger-scale alignment ($0.3\text{--}60 h^{-1}$ Mpc) along the major axis for $L > L_*$ spectroscopic galaxies in the SDSS. And finally, other works (Hawley & Peebles 1975 and MacGillivray et al. 1982) have found isotropic satellite distributions. These results were found using small primary-satellite systems; results with clusters are more definitive, indicating a tendency for the bright cluster galaxy (BCG) to be elongated along the cluster major axis, and hence for it to have satellites concentrated along $\Delta\theta = 0, \pi$ and a deficit at $\pi/2$ and $3\pi/2$, a manifestation of the Binggeli effect (Binggeli 1982; Fuller et al. 1999; West & Blakeslee 2000; Kim et al. 2002). An alignment of physically-associated galaxies with the lens major or minor axis poses a problem for our measurement of f : if there is a larger (smaller) number of physically associated “sources” along the major axis, our azimuthally-averaged boost factor underestimates (overestimates) the signal on the major axis and vice versa for the minor axis, thereby underestimating (overestimating) f . We attempt to measure this effect using a test to be described at the end of this section.

The final effect we consider is the inclusion of galaxies

in the source sample that are actually between us and the “lens,” and that lens the “lens” (foreground contamination). Because this effect causes the “lenses” to have tangential ellipticity relative to the “sources,” it may increase number counts of “sources” along the “lens” minor axis, and decreased number counts along the major axis. Because these foregrounds are not lensed, our boost factor needs to have azimuthal dependence to account for them; since it does not, we may overestimate f . (They also lead to overall suppression of the signal which is unimportant for our f measurement.) Due to our cuts, we do not expect there to be large numbers of foregrounds in our sample, so this effect should not be a major problem, but still test our assumption using the tests described below.

To determine which, if any, of these four possible causes of azimuthally-dependent variations in source density actually occurs, we use the following test. For each lens sample and the sources with photometric redshifts, we divided the lens-source pairs into three samples: the “foreground” sample with $z_s < z_l - \epsilon$ ($\epsilon = 0.05, 0.1$), the “physically associated” sample with $z_l - \epsilon \leq z_s \leq z_l + \epsilon$, and the “source” sample with $z_s > z_l + \epsilon$. Due to photometric redshift errors, these divisions are imperfect. For each of these three samples and lens luminosity/colour samples, we compute the angle-averaged boost-factor $B(r) = N_{LS}/N_{RS}$, where N_{LS} is the number of pairs of real lenses and real sources, and N_{RS} is the number of pairs of random lenses and real sources (with weight equal to 1 for each galaxy), and we also compute the sum over pairs $\xi_{\Delta\theta}(r) = \sum_{LS} e_g \cos(2\Delta\theta)/N_{RS}$.

If we assume that the galaxy density has some isotropic distribution $N_{iso}(r)$ plus a varying component $N_{\Delta\theta}(r)[1 + 2f_{sys}e_g \cos(2\Delta\theta)]$ due to one of the aforementioned effects, then we will have

$$\begin{aligned} B(r) &= [N_{iso}(r) + N_{\Delta\theta}(r)]/N_{RS}(r) \\ \xi_{\Delta\theta}(r) &= 2N_{\Delta\theta}(r)f_{sys}e_{rms}^2/N_{RS}(r) \end{aligned} \quad (23)$$

(the factor of two comes from our use of the full ellipticity e_g^2 , the sum of the squares of the two components, for which $\langle e_g^2 \rangle = 2e_{rms}^2$). Comparing $\xi_{\Delta\theta}(r)$ with $B(r)$ allows us to determine the effective $f_{eff}(r)$ of the distribution of sources, where $f_{eff}(r) = f_{sys}N_{\Delta\theta}(r)/(N_{\Delta\theta}(r) + N_{iso}(r))$ (if the anisotropic component of the number density is much smaller than the total angle-averaged number density, the effect of the anisotropy will be correspondingly smaller). For the two sources of anisotropy $N_{\Delta\theta}(r)$ for which our use of azimuthally-averaged boost factor is incorrect (intrinsic alignments and foregrounds), we will have underestimated f and therefore $f - f_{45}$ by the f_{eff} corresponding to that effect, to lowest order in e . This underestimate can be understood considering that $\Delta\Sigma \propto (1 + 2fe_g \cos(2\Delta\theta))$, but if the boost factor has azimuthal variation, then we really measure shear $\propto (1 + 2f_{\gamma}e_g \cos(2\Delta\theta))$ such that when multiplied by the boost $\propto (1 + 2f_{eff}e_g \cos(2\Delta\theta))$, we get the true $\Delta\Sigma$ ($f_{eff} + f_{\gamma} = f$). When we neglect the f_{eff} of the boost, we therefore underestimate f by this additive factor. However, when we measure $f_{45}\Delta\Sigma_{45} \propto f_{45}e_g \cos(2\Delta\theta)$, to lowest order in e_g there is no correction to account for our use of the azimuthally-averaged boost.

We expect a variation in number density due to magnification bias will appear predominantly on small scales in the “source” sample (most strongly for bright lenses); due to intrinsic alignments, mainly in the “physically associated”

sample but with uncertain scale dependence; due to PHOTO effects in all three source samples equally. but only on small scales; and due to lensing by foregrounds predominantly in the “foreground” sample. Results of these tests will be presented in §5.1.

3.3.3 Shape-shape intrinsic alignments

As mentioned in §3.3.2, physically-associated lens-source pairs may potentially contaminate our measurement due to any shape-shape intrinsic alignments. If the degree of galaxy alignment is independent of $\Delta\theta$, then the shape-shape alignment manifests in the same way as a constant systematic shear, and will be eliminated by the $f\Delta\Sigma - f_{45}\Delta\Sigma_{45}$ subtraction. However, any azimuthal structure in the shape-shape intrinsic alignments would not be removed via this subtraction, and will contaminate the measurement. To test for this problem, we calculate $f\gamma - f_{45}\gamma_{45}$ for sources in the “physically associated” sample (we measure this instead of $f\Delta\Sigma - f_{45}\Delta\Sigma_{45}$ because Σ_c^{-1} is zero for $z_s \leq z_l$). Results of this test are presented in section 5.3.

3.3.4 PHOTO-related shape measurement biases

In principle, the sky brightness systematic may bias the shapes of sources in a way that would affect the measurement of $f\Delta\Sigma - f_{45}\Delta\Sigma_{45}$. This might occur if the sources align with the gradient of the sky brightness near the lenses.

To test for this contamination, we measure $f\gamma - f_{45}\gamma_{45}$ using sources in the “foreground” sample (with $z_s < z_l - 0.1$). This quantity should not have significant contamination from actual lensing or from azimuthal structure in intrinsic alignments, and hence should be dominated by software-related systematics. Results of this test are presented in section 5.4.

4 METHOD OF ANALYSIS

The first step for the halo ellipticity calculation is to compute $\Delta\Sigma$, $f\Delta\Sigma$, and $f_{45}\Delta\Sigma$ as in Eqs. 6 and refE:sums45 and the accompanying text. As described in §3.3.1, $f_{45}\Delta\Sigma$ will allow us to identify systematic shear contributions to $f\Delta\Sigma$. Covariance matrices for these quantities are computed via bootstrap resampling with 150 subregions, similar to the method used in M05. Once we compute these quantities as a function of comoving pair separation r , there are several ways to proceed with the analysis.

The first method used is a non-parametric determination of $f - f_{45}$ averaged over radius. We start with the signal $\Delta\Sigma$ for the desired range of radii, and $f\Delta\Sigma - f_{45}\Delta\Sigma$ with errors determined from those quantities added in quadrature (they are uncorrelated). We then consider the problem of two Gaussian variables y and x that are related via $m = y/x$ (here y represents $f\Delta\Sigma - f_{45}\Delta\Sigma$, x represents $\Delta\Sigma$, and m is our desired quantity, $f - f_{45}$). In our case, we have multiple estimators \hat{y}_i and \hat{x}_i (the values at each radial bin) and would like to combine them while taking into account non-Gaussianity in the ratio \hat{y}/\hat{x} (Bliss 1935a, Bliss 1935b, Fieller 1954). For each measurement i , the quantity $\hat{y}_i - m\hat{x}_i$ is a random Gaussian variable drawn from an $N(0, \sigma_{y_i}^2 + m^2\sigma_{x_i}^2) \equiv N(0, w_i^{-1})$ distribution. Consequently,

the following summation over all measurements is also a random Gaussian variable:

$$\frac{\sum w_i (\hat{y}_i - m \hat{x}_i)}{\sum w_i} \sim N\left(0, \frac{1}{\sum w_i}\right) \quad (24)$$

where the distribution is taken at fixed m , and the weights w_i depend on m . We can then determine frequentist confidence intervals³ at the $Z\sigma$ level by writing

$$\frac{-Z}{\sqrt{\sum w_i}} < \frac{\sum w_i (\hat{y}_i - m \hat{x}_i)}{\sum w_i} < \frac{Z}{\sqrt{\sum w_i}}. \quad (25)$$

Since this expression depends on m , in order to calculate the confidence intervals we make a grid in m and interpolate to find the value of m for the desired confidence interval, e.g. $m(Z = 0)$ corresponds to the average value, $m(Z = \pm 1)$ give the 68 per cent confidence limits, and so on. The value of this approach is that it gives a radius-averaged value of $f - f_{45}$ without requiring a model for the shape of the profile or of $f - f_{45}$, that it easily allows us to combine measurements of $f - f_{45}$ with different source samples for the same lenses, and that it takes into account non-Gaussianity of the error distributions of the ratios \hat{y}_i/\hat{x}_i . Once we have measured $\langle f - f_{45} \rangle_r$ nonparametrically, we relate the result to the predictions for different profiles to extract the value of interest, f_h .

The second method used here is to fit the signal to a power-law profile using the predicted relationships in Eq. 14. That is, we write

$$\Delta\Sigma(r) = Ar^{-\alpha} \quad (26)$$

$$f\Delta\Sigma(r) - f_{45}\Delta\Sigma(r) = Af_h \left[\frac{(\alpha - 2)^2}{4\alpha} \right] r^{-\alpha}$$

and fit jointly for A , α , and f_h . Unlike the previous method, it does not take into account non-Gaussianity in the error distribution of f_h , which we will see is important (and we cannot use this method to measure f_h with the NFW or TIS density profiles).

Finally, we repeat this analysis on large scales (800 h^{-1} kpc to 2 h^{-1} Mpc) with all samples to check for alignment of the light distributions of spirals and ellipticals with local LSS.

5 RESULTS

5.1 Number density systematics

Here we present results related to the azimuthally-dependent boost factor tests described in §3.3. As described there, for “foreground,” “physically associated,” and “source” samples (determined using photometric redshifts), we compute the effective $f_{eff}(r)$ with each of the lens samples; this computation allows us to determine whether magnification bias, PHOTO effects, intrinsic alignments, and lensing by intervening foregrounds may be significant.

For blue lenses of all luminosities, and for L3 and L4 red lenses, $f_{eff}(r)$ was found to be consistent with zero on all scales, as will be discussed further. For red L5 and L6 lenses, this was not the case; a plot of $f_{eff}(r)$ and $B(r)$ for these two lens samples is shown in Fig. 5 with the three source samples.

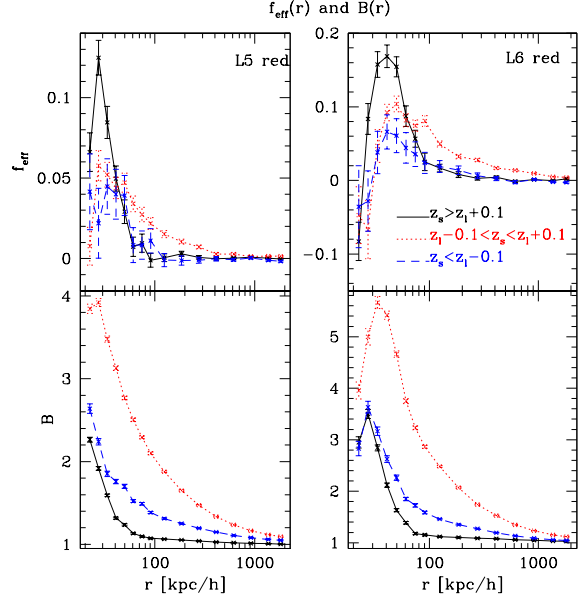


Figure 5. The measured $f_{eff}(r)$ and $B(r)$ for red lenses, L5 and L6, with the three different sets of sources: foregrounds, physically associated, and sources. Note the different scales on the vertical axes for L5 and L6.

There are several important features in this plot. First, we consider the bottom two plots, $B(r)$ for L5 and L6. The fraction of physically associated sources in a given sample is equal to $(B - 1)/B$. So, we see that our photometric redshift cuts are reasonably efficient at isolating a sample of physically associated sources; at 100 h^{-1} kpc, in L6, nearly 2/3 of the “physically associated” sample is actually physically associated, compared to about 15 per cent of the “source” sample and 35 per cent of the “foreground” sample. The fact that $B(r)$ for the physically associated sample actually increases with radius for $20 < r < 30 h^{-1}$ kpc in L5 and $20 < r < 40 h^{-1}$ kpc in L6 indicates that these ranges of radii are affected either by the sky subtraction problem, or by the actual light from the lens galaxy; in any case, due to the possibility of photometric errors in these regions, we exclude them from the analysis in the rest of the paper.

Next, we consider the top plots in Fig. 5, $f_{eff}(r)$ for L5 and L6 red lenses. For L6, we can immediately see that for $100 < r < 2000 h^{-1}$ kpc, $f_{eff}(r)$ is positive for the “physically associated” sample in a way that is highly statistically significant, but not for the other samples. This fact points to density-shape intrinsic alignments as the cause for this finding. Apparently, there is a tendency for satellite galaxies in these ranges of radii to cluster along the major axis of the “lens” galaxy. The results shown here include everything from small groups to large clusters, so what we see is an average of this effect over systems of all sizes. Another work (in preparation) will further explore the luminosity and environment-dependence of this effect in an attempt to understand the cause. This plot shows f_{eff} ; the actual value of f_{int} associated with intrinsic alignments (assuming that the number density on the sky about lenses is isotropic with the exception of this effect) is determined via $f_{eff}(r) = (B(r) - 1)f_{int}(r)/B(r)$. Fig. 6 shows $f_{int}(r)$ for this sample.

³ We are not constructing a Bayesian posterior region $P(m)$.

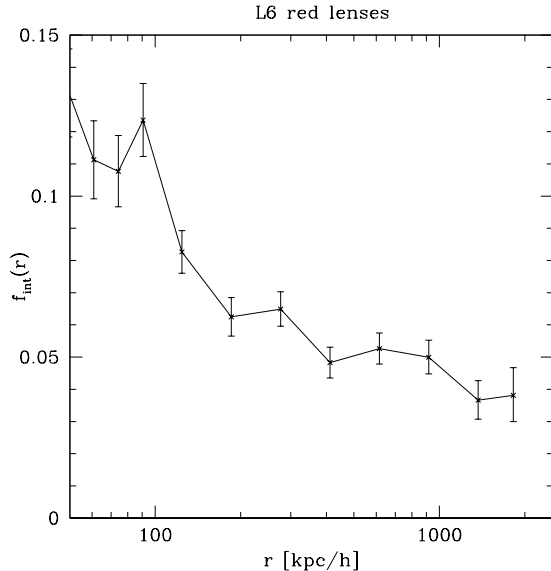


Figure 6. The measured $f_{int}(r)$, including non-Gaussian errorbars, for L6 red lenses derived from the results for physically associated sources

We could also attempt to derive similar results from the foreground or source sample (at least for $r \sim 100 h^{-1}\text{kpc}$, where there is a slight signal) for the sake of comparison. Since $B(r)$ is much lower, $f_{eff}(r)$ due to intrinsic alignments is much lower for these samples. When the results are compared for these radii, the resulting f_{int} is consistent with that shown in Fig. 6 at the 1σ level (we may not expect them to *a priori* be identical, since the samples are different: the physically associated sample includes those with correct photometric redshifts, whereas the foreground and source sample includes physically associated sources with incorrect photometric redshifts, and since they lie in separate regions of colour space, they may have different properties with respect to intrinsic alignments).

For L6, it is clear that on scales larger than $100 h^{-1}\text{kpc}$, the anisotropy of the number density distribution around lenses is due to density-shape intrinsic alignments. Now, we consider scales $r < 40 h^{-1}\text{kpc}$; we already know that the sky subtraction effect or the light of these lenses is causing a loss of number density (as in the $B(r)$ plot), and the rapid decrease in $f_{eff}(r)$ with decreasing r on these scales indicates that the suppression of number density is stronger along the major axis of the lens light distribution, as may be expected. This explanation is supported by the fact that on these scales $f_{eff}(r)$ has roughly the same pattern for all three source samples, and therefore the cause cannot be a physical effect on only foregrounds, physically associated galaxies, or lensed sources. This finding supports our decision to not use these scales when attempting to measure halo ellipticity.

Finally, we consider $40 < r < 100 h^{-1}\text{kpc}$. For this range of radii, $f_{eff}(r)$ changes with r in similar ways for the foreground and physically associated samples; this suggests that it is due to physically associated sources in both, with the amplitude difference being due to the different fraction of physically associated sources in the two samples. However, as r decreases in this range, $f_{eff}(r)$ increases much faster for

the lensed sources; this fact suggests that the increase is due to anisotropy of the magnification bias causing an increase in source number density preferentially along the lens major axis. Unfortunately, the exact f_{eff} for this effect is difficult to extract from the plot due to the unknown radial dependence of the f_{eff} due to intrinsic alignments. We could also attempt to predict it, using the assumed value of $f_{mag}(r)$ for a given profile, with the appropriate $\delta N/N$, to get

$$f_{eff,mag}(r) = f_{mag}(r) \frac{\delta N/N}{B(r)} \quad (27)$$

(The division by $B(r)$ is because we need the ratio of the additional lensed sources to the total number of pairs, not to the total number of lensed pairs which is given by $\delta N/N$.) The difficulty is that it is hard to untangle the effects of f_{int} and f_{mag} in a model-independent way, which means that (1) we cannot easily use the measured f_{mag} as a check on the results for f , and (2) we cannot easily correct the measured f for the effects of f_{int} (since it, but not f_{mag} , contaminates the measurement of f_h).

We can consider several approaches to this problem, but the simplest is to assume that the intrinsic alignments in all three source samples are similar (i.e. there is no colour or magnitude dependence), and therefore to get $f_{eff,int}(r)$ for the lensed sources, we can just use the implied $f_{int}(r)$ from the “physically-associated” sample in Fig. 6 with $B(r)$ to get $f_{eff,int}(r)$ for any source sample. Comparing this prediction against the measured $f_{eff}(r)$ for a given source sample allows us to untangle the effects of f_{int} and f_{mag} .

For L5, the situation is similar, though (1) the small-scale suppression of number counts only extends to $30 h^{-1}\text{kpc}$, not $40 h^{-1}\text{kpc}$, and (2) the detection of ellipticity of the satellite galaxy distribution (density-shape alignment) implied by the nonzero $f_{eff}(r)$ for the physically associated sample is not as large as for L6, though still statistically significant for $r < 400 h^{-1}\text{kpc}$. There is a hint of magnification bias anisotropy on scales up to $70 h^{-1}\text{kpc}$ for this luminosity bin.

The results shown in Fig. 5 imply that we do not observe significant lensing by intervening foregrounds that may have biased our f_h measurement. This may be because the SDSS data are rather shallow.

We now ask how these findings will affect the results with fainter sources as well. There are three effects that we have observed: small-scale effects due to sky subtraction or the lens light distribution causing a loss of sources preferentially along the major axis; effects on all scales due to contamination by physically associated sources that tend to align along the lens major axis; and anisotropic magnification bias for $r < 100 h^{-1}\text{kpc}$ (L6 red lenses), which increases source number density preferentially along the lens major axis. (Since foreground contamination is not a problem for the $r < 21$ sources, at the lowest redshifts, they are certainly not a problem for the fainter, higher redshift source samples.) We consider all three effects separately.

First, we expect that the fainter sources will be affected by the small-scale light problems similarly to the $r < 21$ sources used in this section. Consequently, for these sources we also avoid $r < 30 h^{-1}\text{kpc}$ (L5 red lenses) and $r < 40 h^{-1}\text{kpc}$ (L6 red lenses), but use all scales above $20 h^{-1}\text{kpc}$ for other lens samples.

Second, the $f_{eff}(r)$ due to physically associated sources

is the product of two factors, $f_{int}(r)$ and $(B(r) - 1)/B(r)$. For the fainter sources, $B(r)$ is about 30 per cent higher for the fainter sources (due to the lack of photometric redshift information) than for the brighter ones for $r > 60 h^{-1}\text{kpc}$; below that separation, the difference is not as large. For small boosts as in all luminosity bins for $r > 100 h^{-1}\text{kpc}$ and even for smaller scales for L3 and L4, this translates roughly to a doubling of the $(B(r) - 1)/B(r)$ factor used to determine the f_{eff} . However, it is not clear that the $f_{int}(r)$ for these sources should be the same as for the brighter sources. To determine whether this is a safe assumption, we repeated the tests shown above with $r < 20.3$ and $20.3 < r < 21$ sources separately to check for evolution of f_{int} with apparent magnitude. In both L5 and L6, while $f_{eff}(r)$ and $B(r)$ were different for the $r < 20.3$ and $r > 20.3$ sources, the implied $f_{int}(r)$ values were consistent with each other at the 1σ level for all ranges of radii and all luminosity samples that we use for this analysis. We thus use the same $f_{int}(r)$ for $r > 21$ sources as for $r < 21$ sources; if this is not the case, we will see that the correction we apply is quite small compared to our statistical errorbars. For LRG sources, the lens and source samples are essentially uncorrelated, so contamination by physically associated sources is not a concern.

Finally, the magnification bias effect depends on two things: the magnitude distribution of the source sample, and the R_2 distribution. In M05, we derived that the predicted $\delta N/N$ due to magnification bias is 1.9κ , 0.7κ , and 3.1κ for $r < 21$, $r > 21$, and LRG sources in our catalog, respectively. $\kappa \propto \Sigma_c^{-1}$, which also varies with source sample.

When we actually use the data, we must use the *weighted* (i.e., with weights used for lensing) $B(r)$ and $f_{eff}(r)$ when doing the corrections. The weighted $B(r)$ for the data can be significantly lower than the unweighted, since the Σ_c^{-2} weighting weights higher-redshift sources more heavily, and those sources are less likely to be physically associated with the lenses.

We want to use the weighted $B(r)$ and the angular correlations to determine $f_{eff,int}(r)$, the portion of the anisotropy in the source distribution that is due to contamination by anisotropically-distributed physically-associated pairs, *excluding* the portion of f_{eff} that is due to magnification bias. We then add $f_{eff,int}$ to the measured $f - f_{45}$ to find the non-contaminated value. The correction we calculate is well below the 1σ errors, so too much importance should not be placed on details of the correction scheme, which we outline briefly here. We assume that f_{int} is independent of source sample, and f_{mag} for each sample must be related by consistency relations due to its dependence on the invariant Σ . We fit the f_{int} value to an empirical model (linear in $\log(r)$, which has no theoretical meaning) and extrapolate the values of f_{int} to lower radii to see what $f_{eff,int}$ they predict, assuming that the residual f_{eff} is due to magnification bias.

The resulting $f_{eff,int}(r)$, the amount by which we underestimate the measured $f - f_{45}$ due to our use of the azimuthally-averaged $B(r)$, is then averaged over the range of radii used for the measurement. We find that $f(r) - f_{45}(r)$ is underestimated by 0.01 for $r < 21$ and $r > 21$ sources with L5 red lenses, and by 0.02 for $r < 21$ and 0.03 for $r > 21$ sources with L6 red lenses. Intrinsic alignments are not a significant contaminant for the LRG sources because they are at higher redshifts than the lenses. All of the results in

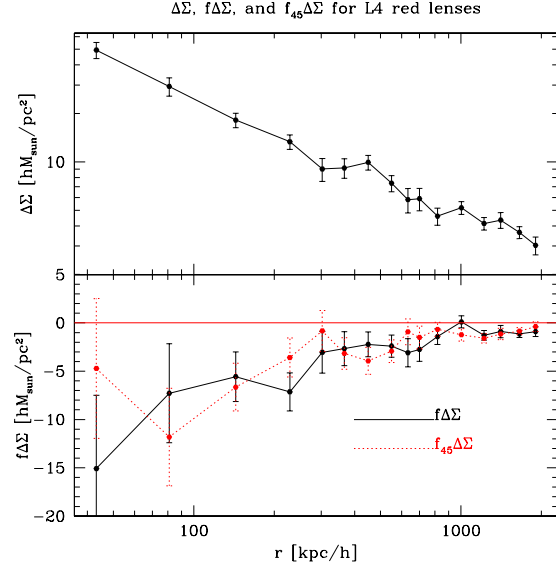


Figure 7. Plot of measured $\Delta\Sigma$ (top), $f\Delta\Sigma$, and $f_{45}\Delta\Sigma$ (bottom) for red L4 lenses with $r < 21$ sources.

the following sections are automatically corrected for this effect.

5.2 Systematic shear

Here we present results for $\Delta\Sigma$, $f\Delta\Sigma$, and $f_{45}\Delta\Sigma$ for the 4 luminosity bins and 2 colour samples. As an example of our findings, Fig. 7 shows these three quantities for L4 red lenses with $r < 21$ sources. As shown, $f_{45}\Delta\Sigma$ is clearly negative at small transverse separations, and becomes closer to zero with increasing radius.

We must then ask what could be causing this signal. There are three possibilities to consider. First, we ask if cosmic shear could be causing this result (i.e. lensing by LSS at redshifts lower than the lens redshifts, causing real alignment of lens and source ellipticities), so that the e_{sys} that we are detecting is an actual effect rather than an artifact of some aspect of the shape measurement. We computed the expected cosmic shear signal for the combinations of lens and source samples with the highest expected cosmic shear signal, assuming the best fit 6-parameter ΛCDM cosmology from Seljak et al. (2005b), the transfer function from Eisenstein & Hu (1998), the growth function from Carroll et al. (1992), and the non-linear mapping from Peacock & Dodds (1996). The results in all cases indicate that cosmic shear is more than 10 times too small to cause the observed lens-source alignment.

Another possibility to consider is that the spurious ellipticity e_{sys} has been imparted to the lenses and sources in the course of PSF correction. The PSF is determined in a given frame ($10'$ by $14'$, or 1489 by 2048 pixels) using ± 2 frames (5 frames total) to determine the Karhunen-Loève (KL) eigenfunctions, then using ± 1 frame (3 total) to do a second-order polynomial fit to the coefficients. With 15–25 stars per frame used to determine the PSF (Lupton et al. 2001), the average separation between stars used to determine the PSF is $\sim 2.6'$. There are a few ways that incorrect PSF determination could cause this effect. The first is sta-

tistical: stars from $r \sim 16$ to 19 are used to determine the PSF. In our source catalog, the error on the ellipticity for a galaxy at $r \sim 19$ is roughly 0.02. If even half of the stars used to determine the PSF are in the range $18 < r < 19$, the statistical error on the PSF ellipticity is of the correct order to cause the effect we see. The spurious ellipticity e_{sys} due to this effect will of course vary randomly from star to star, but since all stars are used to determine the PSF variation across a frame, the statistical error due to a single star may affect a region larger than the separation between stars (since $\theta_{PSF} \sim 300 h^{-1}\text{kpc}$ at the mean effective redshift of the sample in Fig 7).

PSF systematics may also cause this effect; the PSF determination is accurate to within 2 per cent, so systematics in the PSF determination could give rise to some ellipticity of 0.01–0.02. These systematics include the possibility that the spatial change in the PSF is not really quadratic, or strange effects near the edges of the chip.

Now that we know that $f_{45}\Delta\Sigma$ and $f\Delta\Sigma$ are contaminated in similar ways on small scales, our approach must be to use $f\Delta\Sigma - f_{45}\Delta\Sigma$, and compare against model predictions for this quantity on small scales where $\theta \ll \theta_{corr}$, of order a few hundred $h^{-1}\text{kpc}$.

As a further test of the systematic shear subtraction technique, we measured the correlation function of the systematic shear from the data. To do so, we used data from the southern galactic regions, for which there were multiple (> 20) observations of the same area. For 30 pairs of runs in this region (selected randomly), we isolated the set of objects with shape measurements in both runs. For those objects, we then found pairs of galaxies as a function of angular separation. In each run, we computed e_t and e_x for each galaxy in the pair relative to the other, and constructed differences Δe_t and Δe_x for each pair, where the Δ signifies the difference between the values of e_t and e_x in the two runs. Thus, Δe_t and Δe_x encode information about systematic differences in the ellipticities of the same galaxy from run to run. For each pair, we then used the values of Δe_t and Δe_x to construct correlation functions

$$\xi_{++}^{(sys)}(\theta) = \langle \Delta e_{t,1} \Delta e_{t,2} \rangle \quad (28)$$

$$\xi_{xx}^{(sys)}(\theta) = \langle \Delta e_{x,1} \Delta e_{x,2} \rangle \quad (29)$$

$$\xi_{+x}^{(sys)}(\theta) = \langle \Delta e_{t,1} \Delta e_{x,2} \rangle \quad (30)$$

where 1 and 2 denote galaxies in the pair.

Fig. 8 shows the results of this computation, divided by two to approximate the result for the real data, because when comparing the ellipticities across runs, the systematic shear in each of them presumably adds coherently. As shown, $\xi_{++}^{(sys)}$ and $\xi_{xx}^{(sys)}$ are consistent with each other, and $\xi_{+x}^{(sys)}$ is consistent with zero, as expected for any parity-preserving systematic such as spurious ellipticity along the scan direction. Furthermore, the decline of the correlation functions with angular scale indicates that we are correct in our understanding that this is a small-scale systematic. For reference, we note that in L3, the typical radial range used for our calculations ($20\text{--}280 h^{-1}\text{kpc}$) corresponds to $0.0055 < \theta < 0.08$ degrees, and in L6, $40\text{--}320 h^{-1}\text{kpc}$ corresponds to $0.0040 < \theta < 0.03$ degrees. We see from the figure that it is possible that $\langle \Delta e_x \Delta e_x \rangle$ is lower than $\langle \Delta e_+ \Delta e_+ \rangle$ by roughly 5×10^{-5} , and have verified that the resulting changes in the computed values of f_h are significantly less

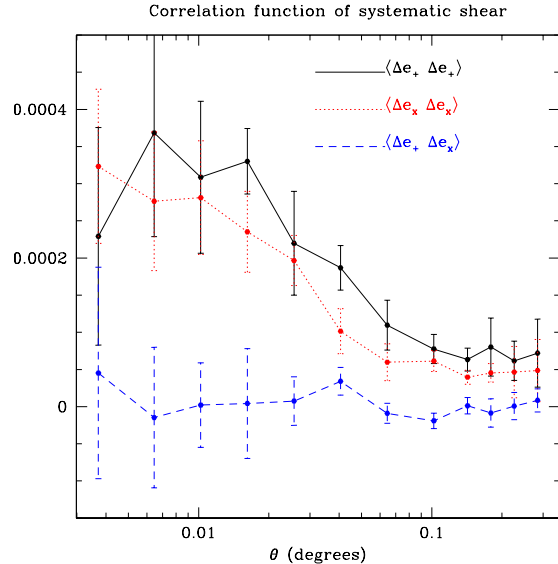


Figure 8. Plot of measured correlation functions of the systematic shear as described in the text.

than half of the 1σ errors for all models, where our overestimate of $\langle \Delta e_x \Delta e_x \rangle$ translates to an overestimate of f_h .

5.3 Shape-shape intrinsic alignments

Here we present results of the calculation of $f\gamma - f_{45}\gamma_{45}$ for the “physically associated” source sample. We then compare the value of $f\gamma - f_{45}\gamma_{45}$ to the observed $\Delta\Sigma$ to see what constraints we can place on the contamination of f_h from azimuthal structure in shape-shape intrinsic alignments, $f_h^{(II)}$.

The resulting $f\gamma - f_{45}\gamma_{45}$ is consistent with zero at the 1σ level for all color and magnitude lens samples, on all scales. This result suggests that the contamination of f_h must be consistent with zero as well; nonetheless, since the predicted values of $f - f_{45}$ for some profiles are so small, we cannot formally place strong constraints on the contamination. For example, for the red lenses, averaged over luminosity, the constraint on $f_h^{(II)}$ is 0.3 ± 0.6 . For the individual luminosity bins, again for the red lenses, the resulting values of contamination are $f_h^{(II)} = 0.0 \pm 1.8, 0.35 \pm 0.81, 0.57 \pm 1.0$, and -0.7 ± 1.7 for L3–L6 respectively.

We note that a recent work (Mandelbaum et al. 2006), indicated no evidence of shape-shape intrinsic alignments on $0.3\text{--}60 h^{-1}\text{Mpc}$ scales using a low-redshift ($z \sim 0.1$) sample of galaxies from the SDSS, despite the detection of a statistically significant density-shape alignment. However, this measurement did not extend below the virial radius, and involved pairs of bright galaxies rather than one relatively bright and one significantly fainter, so we cannot rely solely on it.

5.4 PHOTO-related biases

In this section, we present results of the measurement of $f\gamma - f_{45}\gamma_{45}$ using the “foreground” sample selected using photometric redshifts. Any measurable $f\gamma - f_{45}\gamma_{45}$ should

Table 3. Central values and 68 per cent CL limits on the contamination of f_h due to software biases.

Luminosity sample	$f_h^{(ph)}$ (blue)	$f_h^{(ph)}$ (red)
L3	$3.7_{-5.5}^{+5.7}$	1.3 ± 3.5
L4	$-0.9_{-4.2}^{+4.1}$	-1.0 ± 1.1
L5	-0.6 ± 2.4	-0.9 ± 0.9
L6	$-0.4_{-2.7}^{+2.6}$	$-0.4_{-0.9}^{+0.8}$
All	0.0 ± 1.8	-0.7 ± 0.6

thus be due to software-related biases, e.g. problems in determination of sky brightness or deblending errors.

As for the previous section, we found that the measured $f\gamma - f_{45}\gamma_{45}$ for this sample was completely consistent with zero on all radii, for all lens samples. However, when we compared it against the real $\Delta\Sigma$ for the “source” sample, we found that we cannot place very strong constraints on the contamination of f_h due to photometric errors, $f_h^{(ph)}$. Table 3 shows the constraints for each color and luminosity sample, computed using the SIS profile predictions for $f - f_{45}$ (results with an NFW or TIS model are qualitatively similar).

5.5 Halo ellipticities

Having computed the signal, we proceed with a basic analysis: a non-parametric determination of $f - f_{45}$ averaged over radial ranges for each lens sample and source sample combination, as in §4. There are several considerations for choosing radial ranges: first, we prefer scales small relative to θ_{corr} , so that the $f\Delta\Sigma - f_{45}\Delta\Sigma$ subtraction is justifiable; second, that it is not clear what signal to expect on scales for which neighboring galaxies in the same halo contribute significantly to the lensing signal, so we restrict to radial ranges in which the majority of the weak lensing signal is coming from the lens alone. For L3–L4, we start the measurement from the minimum pair separation used here, $20 h^{-1}\text{kpc}$, and go as far as $245 h^{-1}\text{kpc}$ (L3), and $300 h^{-1}\text{kpc}$ (L4, L5); for L5, we use $30\text{--}300 h^{-1}\text{kpc}$, and for L6, we use $40\text{--}300 h^{-1}\text{kpc}$ because of the small-scale systematics noted in §5.1. The maximum separations are all smaller than θ_{corr} , so the subtraction of $f_{45}\Delta\Sigma$ accurately removes contamination due to systematic shear. Table 4 shows the average $f - f_{45}$ for each lens and source sample combination.

Several results in this table require comment. First, the $f - f_{45}$ values using $r < 21$ sources appear more negative than those for the other source samples, so we must check for consistency of the samples. We do this by finding, for source samples i ,

$$\langle f \rangle_{\text{source}} = \frac{\sum_i f_i / \sigma_i^2}{\sum_i 1 / \sigma_i^2} \quad (31)$$

then getting

$$\chi^2 = \sum_i \left(\frac{(f_i - \langle f \rangle_{\text{source}})^2}{\sigma_i^2} \right) \quad (32)$$

which should follow a χ^2 distribution with degrees of freedom equal to one less than the number of samples being compared. We indeed find that the results with the different samples for each lens sample are statistically consistent.

While the χ^2 test is the most general one that is sensitive to all kinds of discrepancies, the fact that 5 out of the 8 values of f_h for the $r < 21$ sources are lower than for the $r > 21$ sources suggests that we must also devise a test that is more sensitive to a systematic offset. For this test, we compute the eight values of $\delta f = f^{(r < 21)} - f^{(r > 21)}$ and their errors $\sigma(\delta f)$, then find $\langle \delta f \rangle$ via a weighted (by $1/\sigma^2(\delta f)$) average over δf values, and the error on this quantity, $\sigma(\langle \delta f \rangle)$. The result is that the weighted average $\langle \delta f \rangle = -0.13$, with an error $\sigma(\langle \delta f \rangle) = 0.10$. Consequently, the discrepancy is just over 1σ , and therefore not statistically significant.

As shown, the constraints for the blue galaxies are weaker than for the red galaxies. When we average over all source samples for a given luminosity bin for blue galaxies, we find results that are negative for L3–L5 but consistent with zero at the $1 - 1.5\sigma$ level, and for L6, that are positive but again consistent with zero at the 1σ level. For red galaxies, the results are somewhat more complicated. The measured value of $f - f_{45}$ appears to roughly increase with luminosity, which can be explained in several ways, as we will show. We do not show results averaged over lens luminosities, because the results for $f - f_{45}$ must first be related to predictions for $f - f_{45}$ for a given profile to extract the measured f_h for that model, and then averaged over luminosity. In other words, for a given profile, the resulting $f - f_{45}$ for these radial ranges are not the same for different lens luminosities even for the same f_h (due to variation of r_s with luminosity), so an average of $f - f_{45}$ over luminosity is meaningless.

We now relate the non-parametric determination of $f - f_{45}$ in Table 4 to f_h for various halo profiles. However, because our results for $f - f_{45}$ have such large errors, we will not use an extremely detailed or precise model. The simplest model, a SIS, predicts $f/f_h = 0.25$ and $f_{45} = 0$ on all scales, so that for all the results above, we can write $f_h = (f - f_{45})/0.25$. We also consider the NFW and TIS models, but do not attempt to do detailed profile fitting, which is complicated by possible calibration errors due to use of photometric redshifts for foregrounds. What matters is only an approximate value of r_s for the NFW and TIS profiles. To get an approximate value of r_s using the NFW profile, we use best-fit masses for these lens samples from the halo model fits as described in Mandelbaum et al. (2005b) and Seljak et al. (2005a). Since the calibration for the photometric foreground samples is uncertain, we use the same luminosity and colour divisions with the spectroscopic sample lenses, and neglect evolution in the mass-luminosity relationship with redshift (though we do include passive luminosity evolution as noted in §3.1). For the given best-fit mass, we can compute the concentration parameter at the effective redshift of these lens samples using the relationship used in that work and in Mandelbaum et al. (2005b),

$$c(M, z) = 10 \left(\frac{M}{M_{nl}(z)} \right)^{-0.13}. \quad (33)$$

Furthermore, since for an NFW profile the mass and virial radius (where virial mass here is the mass within the radius at which the density is 180 times the mean density, or 54 times the critical density with $\Omega_m = 0.3$) are related, the halo mass and redshift alone determine the scale radii for these luminosity bins. We then used the profile-dependent forms for $f - f_{45}$ in Figs. 1 and 2 to redo the nonparametric

Table 4. Results for $f - f_{45}$ averaged over radial ranges described in the text for each combination of lens and source samples. All errors shown are 68 per cent confidence intervals

Lenses	$r < 21$ sources	$r > 21$ sources	LRGs	all
$f - f_{45}$				
L3, blue	-0.04 ± 0.30	$-0.42^{+0.43}_{-0.48}$	$-2.1^{+2.3}_{-3.0}$	$-0.29^{+0.26}_{-0.27}$
L4, blue	$-0.64^{+0.43}_{-0.48}$	$-0.23^{+0.35}_{-0.36}$	$-0.28^{+0.64}_{-0.70}$	$-0.36^{+0.25}_{-0.26}$
L5, blue	-0.01 ± 0.43	$-0.36^{+0.31}_{-0.44}$	$-0.35^{+0.54}_{-0.58}$	-0.27 ± 0.28
L6, blue	$0.57^{+1.1}_{-0.80}$	$0.77^{+4.0}_{-2.5}$	$1.82^{+1.5}_{-0.9}$	$1.0^{+1.3}_{-0.9}$
L3, red	-0.12 ± 0.21	$-0.51^{+0.20}_{-0.21}$	$-0.25^{+0.23}_{-0.24}$	$-0.33^{+0.12}_{-0.13}$
L4, red	-0.08 ± 0.12	0.07 ± 0.11	0.04 ± 0.15	0.01 ± 0.07
L5, red	-0.19 ± 0.13	0.12 ± 0.12	0.38 ± 0.16	0.08 ± 0.08
L6, red	0.04 ± 0.22	0.34 ± 0.16	0.41 ± 0.24	0.29 ± 0.12

determination of $f - f_{45}$ described above dividing by $(f - f_{45})/f_h$ for our models in each bin, yielding a determination of f_h for these two profiles that includes non-Gaussianity when averaging over these radial bins. For the TIS profile, we fit $\Delta\Sigma$ for the profiles to obtain scale radii only (since the amplitude is a nuisance parameter). Table 5 shows relevant model parameters for the SIS profiles, for the NFW model (M_{180} and r_s), and for the TIS profile (r_s), in addition to the resulting f_h from the non-Gaussian averaging method. We note that the scale radii show the expected trend of increasing with luminosity, and that the best-fit masses are consistent with those from Seljak et al. (2005a) for each bin when we average over the results for each colour.

First, we consider the results for blue lenses in Table 5. With the SIS profile, L3–L5 each have $f_h \sim 1\sigma$ negative, and L6 has $f_h \sim 1\sigma$ positive, yielding a net result of $f_h = -1.1 \pm 0.6$, so almost 2σ negative. We note that the results for each luminosity bin are statistically consistent at the 1σ level, and that the result averaged over luminosity is not equal to that with $1/\sigma^2$ weighting because it includes the non-Gaussianity of the error distributions. With the NFW profile, the measured f_h values are larger in magnitude than with the SIS, as expected due to the lower predicted $(f - f_{45})/f_h$ for this model, and the averaged result is negative but consistent with zero; the same is true for the TIS.

For red lenses, the assumption of an SIS profile gives a net value of $f_h = -0.06 \pm 0.19$, so consistent with no halo ellipticity. However, the NFW and TIS profiles, with lower $(f - f_{45})/f_h$ (even going slightly negative for the TIS), yield positive luminosity-averaged results that are quite similar to each other, 0.60 ± 0.38 (NFW) and 0.57 ± 0.41 (TIS), but again consistent with zero. We note that the errors for the NFW and TIS profiles are larger than for the SIS profile; this is likely due to the fact that the predicted $(f - f_{45})/f_h$ values are so much lower and vary with radius, so since we divide by this small number on large scales, these scales do not dominate as much as they do for the SIS model, where the low measured values of f_h tend to dominate the averaging process and lead to a small result with small errors. For red galaxies, the results in different luminosity bins appear to be statistically inconsistent; use of the χ^2 test for sample consistency in Eq. 32 yields $\chi^2 = 8$ for 3 degrees of freedom, or $p(> \Delta\chi^2) = 0.05$. Hence, while they are not definitively discrepant, there is still a suggestion of either increasing halo

ellipticity, or increasing alignment of halo light and mass with luminosity.

While one might be concerned about the model-dependence of these NFW and TIS predictions, we have verified that for red galaxies, changing the scale radius r_s by 20 per cent in either direction changes the central value of f_h by roughly 0.5σ , so the conclusions we derive from these results are not too strongly sensitive to errors in our derivations of r_s . (For NFW profiles, that change in r_s corresponds to either a 20 per cent change in $c(M, z)$ for a given halo mass, or a 25 per cent change in the halo mass using our assumed $c(M, z)$ relation. For red galaxies, the central halo mass is generally known to this precision or better, as in Table 5.) For blue galaxies, the halo mass is not as well-determined, but neither is $f - f_{45}$, so once again the possible systematic error in f_h due to uncertainty in r_s is within 1σ . Furthermore, since the results with NFW and TIS profiles agree at the 1σ level, it seems that they are not too sensitive to the exact form of the density profile assumed, as long as it is one that is steeper at larger radii, with the scale radius associated with this change increasing with luminosity as we have used here.

Next, we analyzed the results assuming a power-law model for $\Delta\Sigma$, which is approximately true for the scales under consideration, doing a joint fit for the amplitude and slope of $\Delta\Sigma$, and for f_h with $f\Delta\Sigma - f_{45}\Delta\Sigma$. In our case, the amplitude and α are just nuisance parameters, with the important quantity being the best-fit value of f_h . f_h is slightly correlated with α due to the fact that the predicted value of $f - f_{45}$ can be related to a parameter combination including f_h and α . Best-fit values of f_h are shown in table 6; α is typically ≈ 0.8 – 0.9 . The fits were done individually for each lens-source sample combination, and the results were averaged over lens or source samples assuming Gaussian errors. As shown in this table, the results are similar to before in that (1) the results for the $r < 21$ sample are lower than for the other samples, (2) for blue lenses, the results are negative for L3–L5 but positive (with large error) for L6, and (3) for red lenses, the results seem to imply some increase of ellipticity or of alignment of light and mass ellipticities with luminosity. However, as shown here, the values of f_h implied for red lenses are lower than from the NFW and TIS analysis from the non-Gaussian $f - f_{45}$ determination. This is to be expected from our analysis in §2.3, and since the non-power law profiles are more realistic, the results in Table 5

Table 5. Expected values of f_h averaged over radial ranges described in the text, and over source samples for each lens sample, using SIS, NFW and TIS profiles with relevant parameters shown here. Results are also shown averaged over luminosity and colour.

Lenses	SIS profile	NFW profile		TIS profile		
	f_h	M_{180} ($10^{11} h^{-1} M_\odot$)	r_s ($h^{-1} \text{kpc}$)	f_h	r_s ($h^{-1} \text{kpc}$)	f_h
L3, blue	-1.1 ± 1.1	6.1 ± 2.8	16	$-5.2^{+2.7}_{-3.2}$	180	$-2.5^{+1.9}_{-2.1}$
L4, blue	-1.5 ± 1.0	8.9 ± 3.4	19	$-1.7^{+2.5}_{-2.7}$	180	$2.5^{+2.8}_{-2.4}$
L5, blue	-1.1 ± 1.1	9 ± 8	20	$-9.1^{+4.7}_{-5.6}$	250	$-4.6^{+2.7}_{-3.0}$
L6, blue	$4.0^{+5.4}_{-3.6}$	165 ± 246	81	$8.8^{+15.0}_{-7.0}$	400	18^{+11}_{-13}
All, blue	-1.1 ± 0.6	-	-	$-1.4^{+1.7}_{-2.0}$	-	-0.5 ± 1.3
L3, red	-1.3 ± 0.5	5.1 ± 2.5	15	$-5.3^{+2.4}_{-2.8}$	200	$-1.4^{+1.2}_{-1.3}$
L4, red	0.06 ± 0.26	13.0 ± 2.7	23	0.3 ± 0.9	250	0.59 ± 0.62
L5, red	0.31 ± 0.32	67 ± 8	52	0.40 ± 0.57	350	0.47 ± 0.75
L6, red	1.2 ± 0.5	311 ± 82	108	1.7 ± 0.7	600	2.7 ± 1.0
All, red	-0.06 ± 0.19	-	-	0.60 ± 0.38	-	0.57 ± 0.41

Table 6. Results for f_h from power-law profile fits described in the text for each combination of lens and source samples. All errors shown are Gaussian 68 per cent confidence intervals.

Lenses	f_h			
	$r < 21$ sources	$r > 21$ sources	LRGs	all
L3, blue	-6.1 ± 2.7	-1.7 ± 2.0	-3 ± 92	-3.3 ± 1.6
L4, blue	-1.5 ± 1.8	-0.33 ± 0.99	0.0 ± 4.2	-0.6 ± 0.8
L5, blue	-0.29 ± 0.66	-3.5 ± 2.1	-1.4 ± 2.0	-0.7 ± 0.6
L6, blue	13 ± 9	10 ± 11	-0.4 ± 2.0	0.5 ± 1.9
All blue	-0.7 ± 0.6	-1.0 ± 0.8	-0.8 ± 1.3	-0.8 ± 0.4
L3, red	-0.26 ± 0.37	-0.8 ± 0.3	-1.0 ± 1.0	-0.61 ± 0.23
L4, red	-0.16 ± 0.22	0.11 ± 0.18	0.37 ± 0.36	0.05 ± 0.13
L5, red	-0.23 ± 0.22	0.07 ± 0.17	1.7 ± 0.7	0.03 ± 0.13
L6, red	0.01 ± 0.36	0.21 ± 0.08	0.88 ± 0.42	0.21 ± 0.08
All red	-0.17 ± 0.13	0.13 ± 0.07	0.63 ± 0.25	0.10 ± 0.06

are probably more trustworthy. We note that in comparison with the SIS model results in Table 5, the results with this power-law fit method averaged over all sources in the last column of Table 6 (1) are different, and (2) have significantly smaller errors. Considering that the power-law fit model has an additional free parameter (the power-law slope α) which should ostensibly lead to *larger* errors rather than smaller ones, and that the change from $\alpha = 1$ (SIS) to the best-fit values $\alpha = 0.8$ – 0.9 cannot account for the difference in the results, these discrepancies require reconciliation. However, it is important to keep in mind that the method used to determine f_h for Table 5 correctly incorporates the non-Gaussianity of the measurement, whereas the power-law fits used for Table 6 have quoted errors from Gaussian propagation of errors on $\Delta\Sigma$ and $f\Delta\Sigma$; consequently, the larger errors in Table 5 are more likely to be correct. Furthermore, since the use of the non-Gaussian error distributions weights the f_h values in different radial ranges differently than the optimal $1/\sigma^2$ weighting inherent in the χ^2 -minimization power-law fits, it is not surprising that the results from the two methods differ.

5.6 Alignment with LSS

Here we show results for the same tests using $800 h^{-1} \text{kpc}$ to $2 h^{-1} \text{Mpc}$ in order to determine if there is any net alignment

between the ellipticities of the light and of local LSS (e.g., along filamentary structures). For these tests, we assume a power-law profile as is approximately observed on those scales, and use both the non-Gaussian determination and the power-law fit for f_h that assumes Gaussianity of the errors.

The non-Gaussian analysis, averaged over source and lens samples, yields a value of $f_h = -0.46 \pm 0.34$ for spirals, and -0.07 ± 0.09 for ellipticals. As mentioned previously, we expect that for spirals we should see some tendency towards negative f_h on large scales, but unfortunately the errors are too large to be able to confirm this result at this time. For ellipticals, Kim et al. (2002) showed that at least those that are the BCGs of clusters should have their ellipticities aligned with the cluster ellipticity, and therefore we may expect positive f_h for these galaxies; this trend is not observed in this dataset.

The Gaussian analysis (a power-law fit to the signal for amplitude and slope as nuisance parameters in addition to f_h) on these scales yielded $f_h = -0.42 \pm 0.28$ for spirals, and -0.01 ± 0.05 for ellipticals. Hence, both analysis methods yield results that are similar, with a negative result that is not statistically significant for spirals, and a null result that places a constraint on the alignment of light with LSS on 0.8 – $2 h^{-1} \text{Mpc}$ scales for ellipticals.

6 DISCUSSION

We can draw a number of interesting conclusions from the results in §5. First, several of our systematics tests have interesting implications. It is clear that in SDSS data, there are several problems that lead to difficulties in the measurement. The significant systematic shear, which seems to be related to the modeling of the PSF or the PSF correction itself, requires us to undertake additional complications in our analysis (the subtraction of $f - f_{45}$ instead of comparing f directly with the models). Second, small-scale photometric problems lead to loss of sources preferentially along the lens major axis.

Some of the systematics themselves have interesting scientific implications. For example, we have a clear detection of anisotropy of the distributions of satellites around lens galaxies, at least for the brightest red galaxies ($-21 > M_r > -23$). Since many of these galaxies reside in clusters, this may reflect that the BCGs (i.e., our lenses) are aligned with the major axis of clusters, as found by Binggeli (1982) with 44 Abell clusters out to $z = 0.1$, Fuller et al. (1999) with poor, low redshift clusters, West & Blakeslee (2000) in 3 dimensions for the Virgo cluster, and Kim et al. (2002) using ~ 300 clusters in SDSS data over a large range in redshift, $0.04 < z < 0.5$. This effect may be explained in terms of anisotropic infall into the cluster potential well along filaments. An upcoming work will explore this finding in more detail.

Another interesting systematic is the anisotropy of sources due to magnification bias, of which hints were seen in the results, but which was not the focus of this work; future works with higher S/N on the anisotropy of lensing signal and magnification bias, and lower contamination by physically associated sources, should explore the relationship between the two in more detail, since they must be related for consistency to the average dark matter halo profiles and alignment of light and mass ellipticities, and may provide another measure of f_h that will allow for a more precise measurement of halo ellipticity.

Our results for halo ellipticity are not conclusive. For spirals, we appear to have signs of anti-alignment of the ellipticities of light and halo on a $1-2\sigma$ level (when averaged over luminosity) depending on the model used; for ellipticals, we see signs of a progression, with e_h/e_g increasing with luminosity. If we trust the many theoretical predictions of dark matter halo ellipticity (which have been verified by many different types of simulations, both N-body and hydrodynamic), then we must conclude that the trend we see reflects a change in the average alignment of the halo and light ellipticities with luminosity.

We emphasize results with the non-Gaussian averaging over radial ranges rather than the power-law fits that ignore non-Gaussianity in the error distributions, and we emphasize those results using the NFW and TIS models rather than the SIS or other power-law models for $(f - f_{45})/f_h$. Our preference stems from the fact that, while our results in Mandelbaum et al. (2005b) and Seljak et al. (2005a) show that $\Delta\Sigma$ may appear to be a power-law on all scales shown there, $20 h^{-1}\text{kpc}$ to $2 h^{-1}\text{Mpc}$, according to the halo model that is used for the fits to the signal, the signal due to the central halo itself is fit more accurately with an NFW profile (or other truncated profile that falls below the power-law on

several hundred $h^{-1}\text{kpc}$ and larger scales), with the balance of the signal on those larger scales coming from satellites within the same halo for those galaxies that are in a group or cluster. If one assumes that the central halo itself has a power-law density profile, then tries to add in the signal from other galaxies in the group/cluster, the predicted signal becomes too large to fit the data on large scales. Because of the change of the density profile with radius in these more realistic NFW/TIS models, the predicted signal anisotropy on the largest scales probed in this paper ($\sim 300 h^{-1}\text{kpc}$) is significantly smaller than the predicted anisotropy for a power-law profile (with larger error), leading to a significantly larger measured value of f_h using these profiles. We have shown that our results are not very sensitive to even a 20 per cent change in the measured r_s , and are not too different for the NFW or TIS, so they are not too dependent on the parameters of the density profile as long as that density profile roughly matches that of the expected one according to the halo model fits, with a scale-dependent power-law exponent.

There is only one previous measurement of halo ellipticity using weak lensing, Hoekstra et al. (2004). In that paper, the result was that $f_h = 0.77_{-0.21}^{+0.18}$. Our results, while more complicated due to the apparent luminosity dependence, do not seem at first glance to agree with this result. However, we must first ensure that we are comparing the appropriate things, since these two papers use different data and methodology.

There are several differences in the data used for these papers. The SDSS data has redshifts, or at least photometric redshifts with $\sigma(z) \sim 0.04$, for all the lenses used; Hoekstra et al. (2004) uses data from RCS, with redshift distributions only for both lenses and sources. Furthermore, since their lenses have $19 < R < 21$, and mean redshift of 0.35, they correspond mainly to our L4–L6. In this work, we use colour information to approximately separately ellipticals and spirals; Hoekstra et al. (2004) lack that capability, so their results are for a mixture of the two. One might expect that if ellipticals have light and mass ellipticities aligned, and spirals have them anti-aligned, then Hoekstra et al. (2004) should have seen a null result for the mixture, but this is not the case. Indeed, if we average our results (including non-Gaussianity) from Table 5 over luminosities L4–L6 and over colour, we find $f_h = 0.02 \pm 0.21$ for the SIS because it does not take into account predicted radial-dependence of the results, or $f_h = 0.73 \pm 0.39$ for the NFW profile and 0.86 ± 0.43 for the TIS (note that these values are larger than the results averaged over L3–L6 because L3 gives a significantly negative value, and they are positive because the signal for red galaxies entirely dominates over that of the blue galaxies). The latter two results do not actually contradict the result from Hoekstra et al. (2004), so even though we cannot say they constitute a definitive measurement of halo ellipticities, we do not have to worry about a significant discrepancy either. However, we note that this procedure of averaging the f_h values over colour and luminosity, taking into account non-Gaussianity of error distributions, may not give the same answer as the method used in Hoekstra et al. (2004), for which the signals themselves were all averaged and the maximum likelihood method was applied to the average signal. Furthermore, the maximum likelihood method itself is susceptible to bias due

to systematic effects such as the intrinsic ellipticity-density alignment that was observed to be present at some level (but taken into account by a correction factor) in this work. Hoekstra et al. (2004) has a mean lens redshift of 0.35 and mean source redshift of 0.53, whereas this work has a lower mean lens redshift for all luminosities (though the brightest bin is close to that of Hoekstra et al. 2004) and lower mean source redshift for all but the LRG sample. Therefore, if there is some evolution in galaxy ellipticity with redshift, which has been proposed for cluster ellipticities based on simulations in Hopkins et al. (2005), with higher redshift clusters having higher ellipticity, then one might have expected a larger detection in Hoekstra et al. (2004) than here.

The two papers also feature different analysis methods. As argued in an appendix of Hoekstra et al. (2004), they do not expect large systematic shear, though no measurement of f_{45} was presented to show that this is the case. However, systematic shear can only cause an underestimate of f , not an overestimate. Hoekstra et al. (2004) computed the theoretical shear for a TIS model, then introduced anisotropy into the shear (i.e., not into κ and then into the shear via derivation of the full 2-dimensional potential as done here) assuming that the anisotropy is equal to that in a SIS.⁴ Since we have seen that the anisotropy for TIS approaches that of a SIS on small scales, but decreases with scale, the derivation of $f_h = 0.77^{+0.18}_{-0.21}$ is actually an under-estimate, since it assumes the SIS prediction even on larger scales. The fact that the SIS prediction for f/f_h was used means that rather than compare our NFW/TIS predictions against theirs, we must compare our SIS prediction of $f_h = 0.02 \pm 0.21$ against the result of Hoekstra et al. (2004), giving a 2.5σ discrepancy if we take the errors at face value. The Hoekstra et al. (2004) paper derives errors on f_h from the maximum likelihood method, using the $\Delta\chi^2$ values. While this method typically gives reasonable confidence intervals even for non-Gaussian error distributions, the different error derivation between the two results nonetheless means that the apparent 2.5σ discrepancy should not be considered a cause for alarm.

It is clear from this discussion that there are numerous differences between the two works, making the cause for the discrepancy uncertain, the primary contenders being systematic contamination and physical differences of the samples used in the analysis. It is, however, also clear that we do not find a statistically significant alignment between light and dark matter. This may be expected from a theoretical perspective, since the presence of baryons tends to round the dark matter halos (Kazantzidis et al. 2004).

Future work to measure halo ellipticity with galaxy-galaxy weak lensing in the SDSS should have several focuses. First, with time there will be more data, allowing us to increase the signal to noise of these measurements. Second, once there is more data, we will have the ability to characterize the systematics, such as systematic shear and the contamination by intrinsic alignments, better. Finally, we hope in the near future to have a catalog of clusters with ellipticities. Since we are finding hints of a positive detection of halo ellipticity in L6, the most massive lens sample, we hope for more definitive constraints using clusters as lenses,

since they are more massive and the signal-to-noise on their lensing signal is higher than for galaxies.

In conclusion, while we have not made a definitive detection of dark matter halo ellipticity using SDSS data, this work has made several contributions to future efforts in this field. We have identified some of the contaminants to such a measurement that may exist in all datasets, and therefore should be considered in future analyses in this field. We have found suggestions of an anti-alignment of light ellipticities with halo ellipticity on the $1-2\sigma$ level for spiral galaxies (averaged over luminosity), and a suggestion that the light and mass ellipticity alignment in ellipticals is a function of galaxy luminosity, ranging from consistent with zero up to a 2σ alignment in L6. Finally, we have attempted to find correlations between the ellipticities of light and LSS on $0.8-2 h^{-1}\text{Mpc}$ scales, and have placed constraints on such a correlation for ellipticals; results for spirals had fairly large errors so, while the results were negative in accordance with predictions, there is no clear detection. Future efforts with more data should allow us to make more definitive statements about these effects.

ACKNOWLEDGEMENTS

R.M. is supported by an NSF Graduate Research Fellowship. C.H. is supported through NASA grant NGT5-50383. U.S. is supported by Packard Foundation, NASA NAG5-11489 and NSF CAREER-0132953. We thank the referee for many useful suggestions in improving the content and presentation of results.

Funding for the creation and distribution of the SDSS Archive has been provided by the Alfred P. Sloan Foundation, the Participating Institutions, the National Aeronautics and Space Administration, the National Science Foundation, the U.S. Department of Energy, the Japanese Monbukagakusho, and the Max Planck Society. The SDSS Web site is <http://www.sdss.org/>.

The SDSS is managed by the Astrophysical Research Consortium (ARC) for the Participating Institutions. The Participating Institutions are The University of Chicago, Fermilab, the Institute for Advanced Study, the Japan Participation Group, The Johns Hopkins University, the Korean Scientist Group, Los Alamos National Laboratory, the Max-Planck-Institute for Astronomy (MPIA), the Max-Planck-Institute for Astrophysics (MPA), New Mexico State University, University of Pittsburgh, University of Portsmouth, Princeton University, the United States Naval Observatory, and the University of Washington.

REFERENCES

- Abazajian K. et al., 2003, AJ, 126, 2081
- Abazajian K. et al., 2004, AJ, 128, 502
- Abazajian K. et al., 2005, AJ, 129, 1755
- Bernstein G. M., Jarvis M., 2002, AJ, 123, 583
- Binggeli B., 1982, A&A, 107, 338
- Blanton M. R., et al., 2003a, AJ, 125, 2348
- Blanton M. R., et al., 2003b, ApJ, 592, 819
- Bliss C. I., 1935a, Ann. Appl. Biol., 22, 134
- Bliss C. I., 1935b, Ann. Appl. Biol., 22, 307

⁴ H. Hoekstra, e-mail communication.

- Brainerd T. G., 2004, *ApJ*, 628L, 101
- Brainerd T. G., Blandford R. D., Smail I., 1996, *ApJ*, 466, 623
- Carroll S. M., Press W. H., Turner E. L., 1992, *ARA&A*, 30, 499
- Coil A. L. et al., 2004, *ApJ*, 609, 525
- Cooray A., Sheth R., 2002, *Phys.Rep.*, 372, 1
- Davis M. et al., 2003, in *Proceedings of the SPIE*, Volume 4834, pp. 161-172
- Davis M., Gerke B. F., Newman J. A., 2004, preprint (astro-ph/0408344)
- Dubinski J., Carlberg R. G., 1991, *ApJ*, 378, 496
- Eisenstein D. J., Hu W., 1998, *ApJ*, 496, 605
- Eisenstein D. J. et al., 2001, *AJ*, 122, 2267
- Fieller E. C., 1954, *J. R. Stat. Soc. B*, 16, 175
- Fischer P. et al., 2000, *AJ*, 120, 1198
- Fuller T. M., West M. J., Bridges T. J., 1999, *ApJ*, 519, 22
- Fukugita M., Ichikawa T., Gunn J. E., Doi M., Shimasaku K., Schneider D. P., 1996, *AJ*, 111, 1748
- Gunn J. E. et al., 1998, *AJ*, 116, 3040
- Guzik J., Seljak U., 2002, *MNRAS*, 335, 311
- Hawley D. L., Peebles P. J. E., 1975, *AJ*, 80, 477
- Hirata C., Seljak U., 2003, *MNRAS*, 343, 459
- Hoekstra H., Franx M., Kuijken K., Carlberg R. G., Yee H. K. C., 2003, *MNRAS*, 340, 609
- Hoekstra H., Yee H. K. C., Gladders M. D., 2004, *ApJ*, 606, 67
- Hogg D. W., Finkbeiner D. P., Schlegel D. J., Gunn J. E., 2001, *AJ*, 122, 2129
- Holmberg E., 1969, *Arxiv Astron.*, 5, 305
- Hopkins P. F., Bahcall N. A., Bode P., 2005, *ApJ*, 618, 1
- Hudson M. J., Gwyn S. D. J., Dahle H., Kaiser N., 1998, *ApJ*, 503, 531
- Ivezić Ž. et al., 2004, *Astronomische Nachrichten*, 325, 583
- Kazantzidis S., Kravtsov A. V., Zentner A. R., Allgood B., Nagai D., Moore B., 2004, *ApJ*, 611, L73
- Keeton C. R., 2001, preprint (astro-ph/0102340)
- Kim R. S. J., Annis J., Strauss M. A., Lupton R. H., 2002, in *ASP Conf. Ser.* 268, p. 395
- Kleinheinrich M. et al., 2005, *A&A*, 439, 513
- Libeskind N. I., Frenk C. S., Cole S., Helly J. C., Jenkins A., Navarro J. F., Power C., 2005, *MNRAS*, 363, 146
- Lupton R. H., Gunn J. E., Ivezić Z., Knapp G. R., Kent S., Yasuda N., 2001, in *ASP Conf. Ser.* 238, p. 269
- MacGillivray H. T., Dodd R. J., McNally B. V., Corwin H. G., 1982, *MNRAS*, 198, 605
- Madgwick D. S. et al., 2003, *ApJ*, 599, 997
- Mandelbaum R., et al., 2005a, *MNRAS*, 361, 1287
- Mandelbaum R., Tasitsiomi A., Seljak U., Kravtsov A. V., Wechsler R. H., 2005b, *MNRAS*, 362, 1451
- Mandelbaum R., Hirata C., Ishak M., Seljak U., Brinkmann J., 2006, *MNRAS*, 367, 611
- McKay T. A. et al., 2001, preprint (astro-ph/0108013)
- Milgrom M., 1983, *ApJ*, 270, 365
- Natarajan P., Refregier A., 2000, *ApJ*, 538, L113
- Navarro J. F., Frenk C. S., White S. D. M., 1996, *ApJ*, 462, 563+
- Navarro J. F., Abadi M. G., Steinmetz M., 2004, *ApJ*, 613, L41
- Padmanabhan N. et al., 2005, *MNRAS*, 359, 237
- Peacock J. A., Dodds S. J., 1996, *MNRAS*, 280, L19
- Pier J. R., Munn J. A., Hindsley R. B., Hennessy G. S., Kent S. M., Lupton R. H., Ivezić Ž., 2003, *AJ*, 125, 1559
- Richards G. T. et al., 2002, *AJ*, 123, 2945
- Sackett P. D., 1999, in *ASP Conf. Ser.* 182, p. 393.
- Sales L., Lambas D. G., 2004, *MNRAS*, 348, 1236
- Sanders R. H., 1986, *MNRAS*, 223, 539
- Sanders R. H., McGaugh S. S., 2002, *ARA&A*, 40, 263
- Seljak U. et al., 2005a, *Phys.Rev.D*, 71, 043511
- Seljak U., et al., 2005b, *Phys.Rev.D*, 71, 103515
- Sheldon E. S. et al., 2004, *AJ*, 127, 2544
- Smith D. R., Bernstein G. M., Fischer P., Jarvis M., 2001, *ApJ*, 551, 643
- Smith J. A. et al., 2002, *AJ*, 123, 2121
- Stoughton C. et al., 2002, *AJ*, 123, 485
- Strateva I. et al., 2001, *AJ*, 122, 1861
- Strauss M. A. et al., 2002, *AJ*, 124, 1810
- West M. J., Blakeslee J. P., 2000, *ApJ*, 543, L27
- Wright C. O., Brainerd T. G., 2000, *ApJ*, 534, 34
- York D. G. et al., 2000, *AJ*, 120, 1579
- Zaritsky D., Smith R., Frenk C. S., White S. D. M., 1997, *ApJ*, 478, L53
- Zentner A. R., Kravtsov A. V., Gnedin O. Y., Klypin A. A., 2005, *ApJ*, 629, 219